LIGO Photodiode Characterization and Measurement of the Prestabilized Laser Intensity Noise

by

Peter Csatorday

Submitted to the Department of Physics in partial fulfillment of the requirements for the degree of

Master of Science

at the

MASSACHUSETTS INSTITUTE OF TECHNOLOGY

September, 1999

Author .....
Department of Physics
August 1999

Certified by .....
Rainer Weiss
Professor of Physics
Thesis Supervisor

Accepted by .....
Thomas J. Greytak
Professor, Associate Department Head for Education
Department of Physics

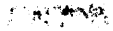

LIGO Photodiode Characterization and Measurement of the Prestabilized Laser Intensity Noise

by

Peter Csatorday

Submitted to the Department of Physics September 1999 in partial
fulfillment of the requirements for the degree of
Master of Science

Abstract

The Laser Interferometer Gravitational Wave Observatory (LIGO) and other current generation laser interferometer gravitational wave antennas have demonstrated the need for photodetector performance that neither existing commercial, nor laboratory prototype devices have met. We undertook the development of a new detector whose parameters were dictated by the expected conditions at the "dark", or "antisymmetric", port of the interferometer — where the actual length sensing signals that provide a measurement of the gravitational wave strain are read out.

LIGO is a recycled Michelson interferometer with Fabry-Perot arm cavities. Length sensing and control of the arm lengths works by radio frequency optical modulation and homodyne demodulation techniques. The carrier is a beam of Nd:YAG laser light. To maximize the gravitational signal-to-noise ratio, one uses high laser power in the interferometer and expects about 600mW to appear at the dark port. The detection elements are photodetectors with reverse biased photodiodes followed by low-noise voltage amplification stages. The above constraints, namely high power and near infra-red wavelength (1.064 μm), and the need to maximize quantum efficiency require the use of InGaAs photodiodes. Further considerations in the diode selection process are diode capacitance and area, linearity, detector uniformity, backscatter, reflectivity and thermal impedance.

Another important requirement of LIGO is the limit placed on the power fluctuations of light at radio frequencies, particularly at the modulation frequency of the length sensing system mentioned above. We measure the power spectral density of these fluctuations at the first installed laser subsystem (the 'Pre-stabilized' laser, or PSL) using a variant of our detector design.

This thesis describes the tests that were performed on commercially available photodiodes used in our detectors, the motivation for these tests, and their relevance to the circuit design. We also describe an adaptation of the resulting instrument for the purpose of measuring the intensity fluctuations of the LIGO laser and the results of these measurements.

Thesis Supervisor: Rainer Weiss
Title: Professor of Physics

Table of Contents

List of Figures

List of Tables

List of Acronyms and Abbreviations

AFM	Atomic Force Microscope
AM	Amplitude Modulation
AOM	Acousto Optic Modulator
AR	Anti-Reflection
BRDF	Bidirectional Reflectance Distribution Function
CCD	Charge Coupled Device
CDD	Conceptual Design Document
DRD	Design Requirements Document
EG&G	EG&G Inc. (manufacturer)
EOM	Electro-Optic Modulator
ETM	End Test Mass
FDD	Final Design Document
GPD	Germanium Power Devices (manufacturer)
InGaAs	Indium Gallium Arsenide
ISS	Intensity Servo System
ITM	Input Test Mass
LIGO	Laser Interferometer Gravitational Wave Observatory
LSC	Length Sensing and Control
MO	Master Oscillator
MOPA	Master Oscillator Power Amplifier
Nd:YAG	Neodymium Yttrium-Aluminum-Garnet
PDH	Pound-Drever-Hall
PMC	Pre-modecleaner
PSL	Prestabilized Laser
QE	Quantum Efficiency
RF	Radio Frequency
VCO	Voltage Controlled Oscillator
VIRGO	French-Italian collaboration for interferometric gravitational wave detection.

Chapter 1

Introduction

1.1 Gravitational Waves and LIGO

One of the consequences of the theory of general relativity is the existence of gravitational waves, perturbations of space-time that travel at the speed of light [Einstein '16][Einstein '18]. Direct detection of these waves has been the elusive goal of experimenters for close to four decades now. However, recent advances and construction of large scale detectors give the community hope that the time is near when not only detection is possible, but useful astrophysical observations can be made with gravitational waves [Weiss '99].

In the weak field limit, as is the case for all Earth based observations, one can linearize the equations of general relativity and write the space-time metric, $g_{\mu\upsilon}$, as the sum of the flat space Minkowski metric, $\eta_{\mu\upsilon}$, and a small perturbation, $h_{\mu\upsilon}$:

$$g_{\mu\upsilon} \approx \eta_{\mu\upsilon} + h_{\mu\upsilon} \tag{1.1}$$

where $|h_{\mu\upsilon}| \ll 1$. In this limit, in a source-free region, the perturbation obeys the wave equation

$$\left(-\frac{1}{c^2}\frac{\partial^2}{\partial t^2} + \nabla^2\right) h_{\mu\upsilon} = 0 \tag{1.2}$$

The solutions are transverse plane waves. For instance, in the transverse traceless gauge (coordinate system) for a gravitational wave traveling in the $\hat{z}$ direction,

$$h_{\mu\upsilon} = e^{i(\omega t - k_i x^i)} \begin{bmatrix} 0 & 0 & 0 & 0 \\ 0 & h_+ & h_x & 0 \\ 0 & h_x & -h_+ & 0 \\ 0 & 0 & 0 & 0 \end{bmatrix} \tag{1.3}$$

This solution exhibits two independent modes of the metric; these are referred to as the "plus" and "cross" polarizations. For the "plus" solution, at a given point along the $\hat{z}$ axis, space in the $\hat{x}$ direction is expanded and contracted at the frequency of the gravitational wave. The same happens in the $\hat{y}$ direction, but with a half-cycle phase delay, so that while $\hat{x}$ contracts, $\hat{y}$ expands, and vice-versa. The "cross" polarization behaves in exactly the same way, but its basis directions are at a 45 degree angle relative to those of the "plus". The magnitude of expansion can be calculated by integrating the metric along the direction that is changing; one finds that the change in length is proportional to the length itself (constituting a strain), the constant of proportionality being one half the magnitude of the metric perturbation:

$$\frac{\delta l}{l} = \frac{1}{2}h_{+} \tag{1.4}$$

This expanding and contracting of space is well suited for measurement by a Michelson-type interferometer with perpendicular arms. As one arm expands, the phase of the light in it returning to the beamsplitter is delayed, while as the other contracts, the phase of light in that arm is advanced. The resulting phase difference causes a change in the interference pattern, or fringe, at the output of the interferometer. If we operate the interferometer such that normally there is no light exiting the output port (destructive interference) then any gravitational perturbation (wave) will result in a differential arm-length change and manifest itself as light at the output. The key is that the lengths of the arms have to be controlled accurately to begin with; this is the task of the Length Sensing and Control (LSC) subsystem in LIGO. Furthermore, because in practice the lengths are always kept as constant as possible using active servo loops, evidence of gravitational waves will be found in the error signals of the LSC servos.

Lastly, we note that since the phase advance or delay is proportional to the distance traveled by light in an arm, one tries to maximize the optical path length by using long arms (4km for LIGO) and by bouncing the light back and forth many times. This latter technique can be done with delay lines, but is usually accomplished using Fabry-Perot cavities. One also tries to maximize the power incident on the interferometer to achieve more optimal signal-to-noise performance, and for this LIGO places a partially transmitting mirror at the input port so that light that would leave the interferometer there is sent back. These considerations lead to the interferometer topology of figure 1.1, known as a power recycled, Fabry-Perot arm cavity, Michelson interferometer.

1.2 Length Sensing and Control

As mentioned above, the interferometer arm lengths have to be controlled to high precision in order to keep the light resonating in the arm cavities and the recycled Michelson interferometer. There turn out to be five degrees of freedom in the problem: the arm cavity lengths, the differential and common mode lengths of the Michelson, and the laser wavelength. This last quantity can be controlled through the prestablizied laser (PSL, described in section 1.4). The mirrors and beamsplitters are suspended in vacuum so that they approximate freely falling test masses at frequencies above the natural resonances of the suspensions. Their positions are adjusted with magnetic actuators that push or pull on fins attached to the optics. The control signals for these actuators are provided by the LSC and are derived from photodetector sensors at pick-offs at the reflected and recycling cavity ports and by detectors at the dark port of the interferometer (figure 1.1). The techniques for sensing the lengths are a combination of Schnupp modulation [Schnupp '86] and Pound-Drever-Hall (PDH) locking [Drever '83]. They both rely on radio frequency (RF) phase modulation impressed on the laser light by a Pockels cell and either length asymmetries or complex reflectivity changes to bring about a beat signal between the carrier and the sidebands.

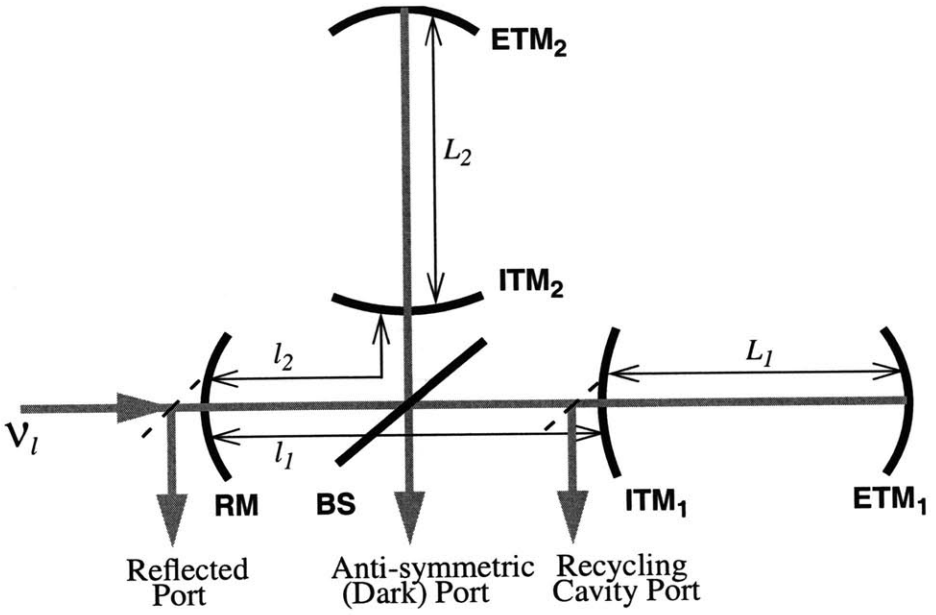

Figure 1.1: LIGO Interferometer with lengths relevant to LSC. Abbreviations are: BS: Beamsplitter, RM: Recycling Mirror, ITM: Input Test Mass, ETM: End Test Mass.

This beat is an amplitude modulated signal that is sensed with our photodetectors and electronically demodulated, or "mixed down"; hence the need for fast photodetectors. The magnitude of the mixed down signal is indicative of deviations from optimal positions of the test masses.

1.3 Photodetectors

The length sensing method mentioned in the previous section clearly shows the need for photodetectors capable of detecting signals at RF frequencies. The modulation frequencies in LIGO are 24.463 MHz and 29.449 MHz, for the 4 km and 2km arm length interferometers, respectively. The standard design for such detectors is a reverse biased photodiode in series with a tuned inductor. This forms a resonant circuit that enhances the impedance and consequently the signal-to-noise ratio at the resonant frequency. The light in the interferometer will also contain modulation at twice the fundamental frequency and unwanted signals from this are attenuated by putting a notch filter in the electronics. The design is schematically shown in figure 1.2 and a near final LIGO circuit design is in figure A.2.

The guiding requirement in designing the detector was that the signal be at least a factor of ten higher than the electronics noise of the circuit. The signal level for the purposes of this design is the shot noise of the photocurrent; this is a lower bound on any measurable optical signal. Both noise and signal are dependent on the resonant impedance of the circuit, Z_R. The noise is made up of Johnson (thermal) noise of the impedance, the voltage noise of the amplifier, e_n, and the current noise of the amplifier, i_n, generating a voltage across the resonant impedance. These

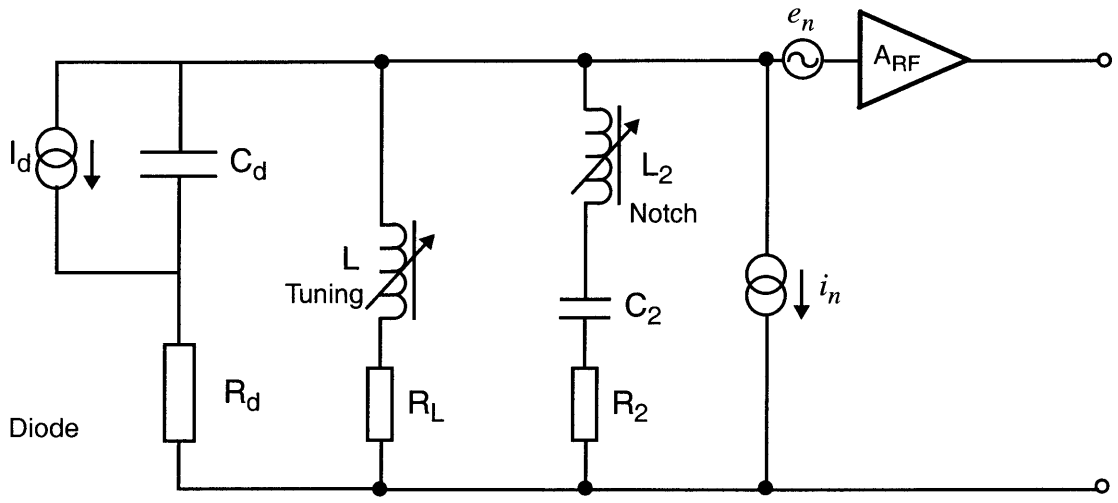

Figure 1.2: Simplified photodiode-preamp equivalent RF circuit. The series L2-C2 notch is tuned for $2f_R$ and the inductor L is tuned to give a resonance at f_R; R_L and R_2 are included to account for losses in the inductors. e_n and i_n are the amplifier equivalent voltage and current noise generators.

terms add in quadrature, so the total noise is $e_\Sigma^2 = e_n^2 + i_n^2 Z_R^2 + 4kTZ_R$, with the last term giving the dominant contribution at room temperature. The shot noise is $e_{shot}^2 = 2q\bar{I}Z_R^2$, where $\bar{I}$ is the average photocurrent. Using these definitions, the signal-to-noise requirement can be restated as $e_{shot}/e_\Sigma \geq 10$. The key point here is that our signal-to-noise ratio improves as the resonant impedance increases; this in turn is dependent on the diode equivalent capacitance, making that an important quantity to minimize. The measured resonant impedance turns out to be $Z_R \approx 225\Omega$ (section 2.7.1) and the amplifier noise terms are e_n = 0.75 nV/$\sqrt{\text{Hz}}$ and i_n = 1.2 pA/$\sqrt{\text{Hz}}$. These values mean that the minimum photocurrent meeting our requirement is 26.5 mA. We find, fortunately, that the diodes are able to operate at much higher currents (chapter 2) and for the 600mW expected optical power at the dark port, we shall employ four detectors each with just in excess of 100mA of photocurrent. This level should also ensure adequate margin in the signal-to-noise ratio to overcome noise added after the detector circuit, correlations between the noise sources (not considered above), and the nonstationarity of the photocurrent. In chapter 3 we describe similar considerations for building a broadband detector that does not use a resonant circuit.

So far, we have mentioned only one important diode parameter, the capacitance, that we needed to consider for our application. In chapter 2 we give a more complete list of tests and considerations that narrowed our choice to the EG&G 2mm diameter Indium-Gallium-Arsenide (InGaAs) article.

1.4 Prestabilized Laser

The Prestabilized Laser (PSL) is the LIGO subsystem responsible for providing the light entering the interferometer. The light must meet stringent requirements on amplitude and phase

noise, power, beam shape and mode content, and beam jitter [PSL DRD]. The PSL is located on a single optical table outside the vacuum system. Its main components are a Lightwave Electronics 10 Watt Nd:YAG master-oscillator power-amplifier (MOPA) laser; a thermally stabilized, suspended, vacuum enclosed, fused silica reference cavity for frequency stabilization; a triangular cavity for passive intensity noise filtering and beam shaping, called the Pre-Modecleaner (PMC); and an acousto-optic modulator based active intensity noise servo used at low frequencies (ISS). There is also an input for controlling the laser frequency from an external source (the "wideband input"), which allows one to use a full 4km LIGO arm cavity as a stable frequency reference (figure 1.3 and [PSL FDD]).

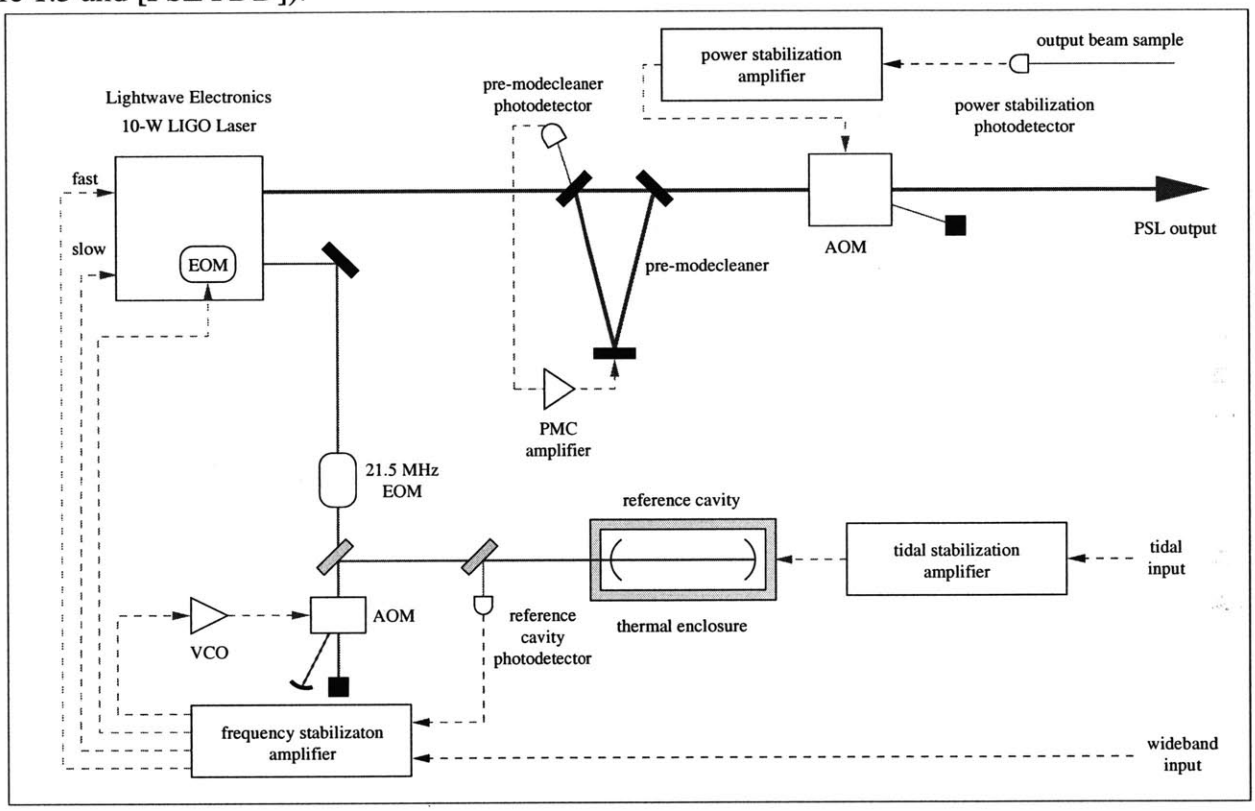

Figure 1.3: PSL Optical Schematic.

Of the requirements mentioned above, we concern ourselves with the power fluctuations at the RF modulation frequencies. These are required to be less than 1.005 times the fluctuations due to shot noise in a 600mW beam, or in other words, the excess noise should be at least 10dB below the shot noise in a beam of light carrying the power expected at the dark port. Note that this requirement allows for much more noise than if one were to expect the excess noise to be 10dB below the shot noise fluctuations of the full PSL output (since we are dealing with relative fluctuations). The root of this requirement lies in the fact that fluctuations in the difference in arm lengths ($\delta(L1 - L2)$, in figure 1.1) couple with radio frequency laser power fluctuations to produce gravitational wave band noise. [LSC DRD] [Sigg '97]

Chapter 2

Characterization of Photodiodes

2.1 Introduction

We tested many photodiodes from commercial manufacturers for possible use in LIGO. These included 1 mm, 2 mm and 3 mm diameter InGaAs diodes from Hamamatsu, 2 mm and 3 mm diameter InGaAs diodes from EG&G and GPD, and even a germanium diode from GPD. Rather than give an exhaustive account of the test results for the various diodes, we focus in this chapter on describing the actual tests and show results for only selected diodes. In some instances early tests would rule out a given candidate or the manufacturer would provide more detailed information, so not all diodes were subject to all experiments. For a more complete account, the reader is referred to LIGO document T-980016-00 [LSC Photodiode]. Often it is hard to assess diode performance independently of the circuit it is in; in the last section of this chapter we report on some tests performed on an early LIGO production detector unit.

2.2 Electro-Optical Properties

Figure 2.1 presents the optical setup used for our photodiode evaluations. The laser is a Lightwave Electronics model 126, with adjustable power up to 700mW, of which a maximum of about

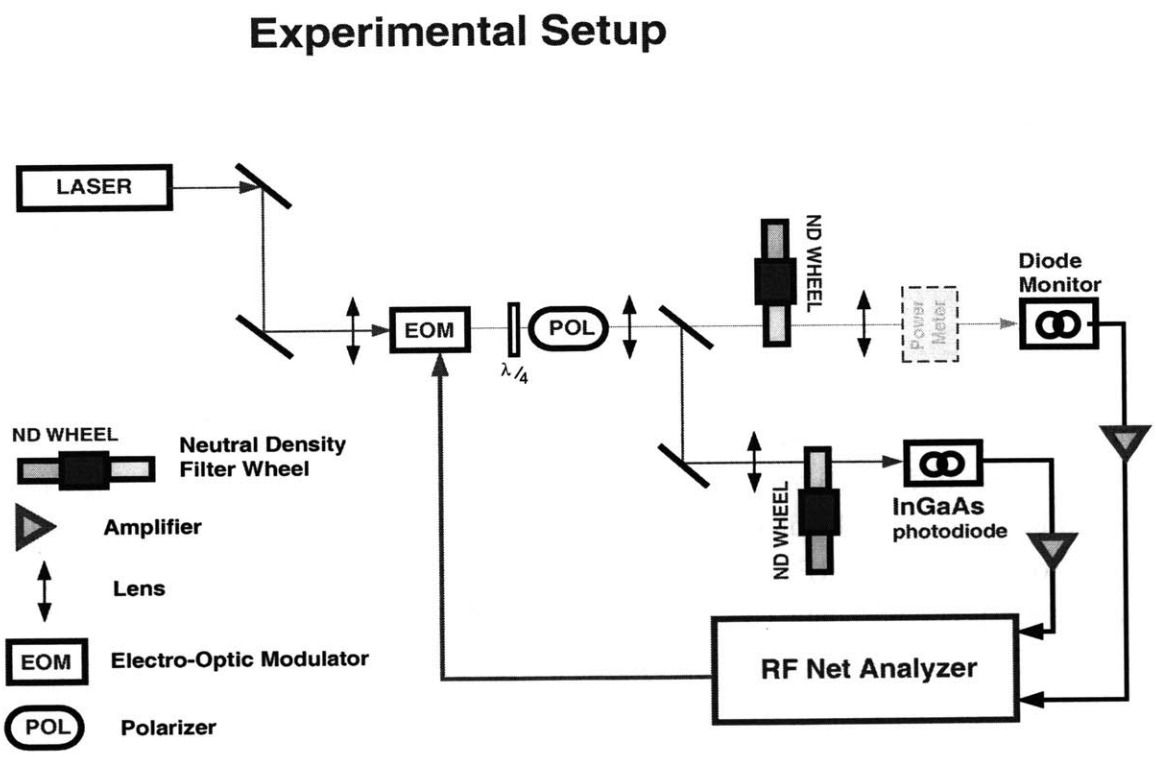

Figure 2.1: Photodiode Test setup

200mW could reach the diode under test. The broadband electro-optic modulator (EOM) applies phase modulation to the light which the quarter-wave plate and polarizing beamsplitter convert to amplitude modulation. The amount of modulation is controlled by the drive power to the EOM and the light intensity is adjusted with the neutral density filters. We remove the windows from the TO-5 packages that all diodes come shipped in.

2.2.1 Quantum Efficiency

Quantum efficiency (QE) is the number of photoelectrons per incident photon generated in the photodiode. This quantity is highly spectrally dependent, at long wavelengths predominantly determined by the semiconductor bandgap. We measure a related quantity, known as the responsivity, which is the photocurrent generated per incident radiant power. At a wavelength of 1064 nm, $QE = 1.16R$, where R is the responsivity in A/W and the quantum efficiency is expressed as a percentage. We also distinguish between "internal" and "external" quantum efficiency: internal is given by the semiconductor physics whereas "external" is the overall photon to electron conversion efficiency, taking into account all losses due to reflection, scattering, etc.

To measure the responsivity, we mount the diode in a test circuit (figure A.1) used to apply reverse bias to the diode and to read out the DC current. We shine the laser on the diode and measure the incident and specularly reflected power using a calibrated power meter. This gives for a typical InGaAs diode, a responsivity of 0.71 A/W, or a QE of 82%. The uncertainty is about 3%, mostly due to the power meter calibration.

LIGO requirements call for a net quantum efficiency of 80% from the beamsplitter to the detection electronics. The current estimate for this is 79.3%, with most of the loss coming from the photodiodes [LSC FDD].

2.2.2 Spatial Uniformity

The LIGO requirement for the uniformity of response over the diode surface is that variations should be less than 2% RMS over the spatial scale of the beam [LSC DRD] to preserve modal orthogonality [Zucker '98].

We measure the nonuniformity by reducing the test laser beam diameter to 150μm, mounting the photodiode test assembly on a two axis stage and scanning over a 10 by 10 grid of points, recording both the DC and RF responses. The results of these measurements for the 2mm Hamamatsu diode (G5832-2) are presented in figure 2.2. The two observed dips in response are believed to be inherent to the diode, perhaps due to construction or structural reasons. They are present in both the DC and RF measurements. Even with these defects, the nonuniformity of the 2mm Hamamatsu is better than 1.2%. Measurements of the 3mm Hamamatsu diode (G5832-3), indicate an RF spatial nonuniformity of about 3.2%, primarily due to enhanced response near the edges (figure 2.3). The 2mm and 3mm diameter EG&G also show good spatial uniformity, confirming the manufacturer's measurements.

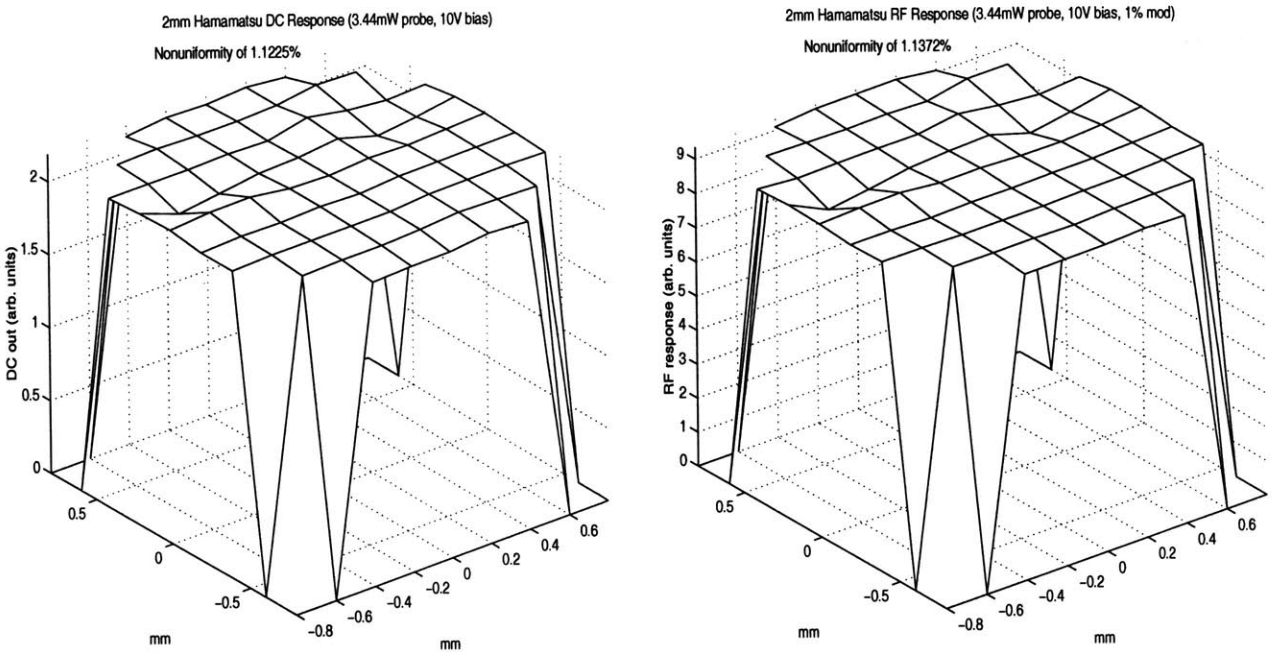

Figure 2.2: DC and RF spatial uniformity of the G5832-2 diode

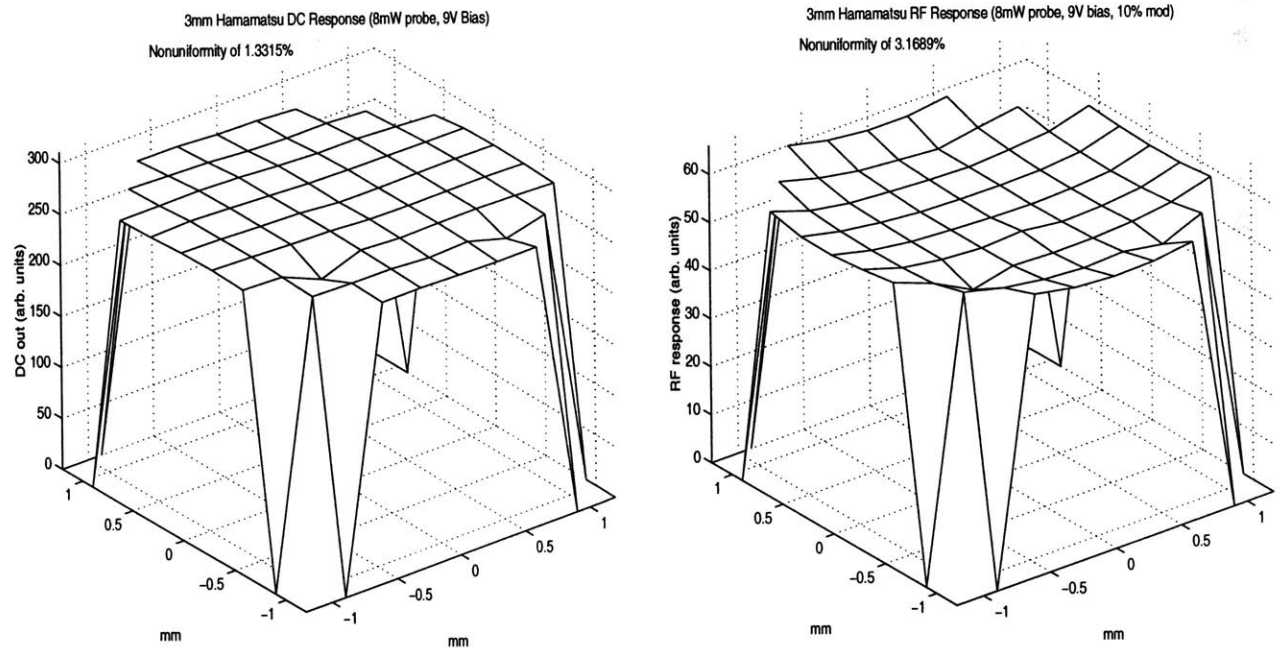

Figure 2.3: DC and RF spatial uniformity of the G5832-3 diode

2.2.3 Response Dependence on Bias Voltage

Higher reverse bias voltages give rise to more linear diode behavior (as well as lower junction capacitance). Figures 2.4 and 2.5 show, respectively, the dependence of the DC and RF response on bias voltage for the 2mm Hamamatsu diode. For the RF measurement, a 1% modulation was

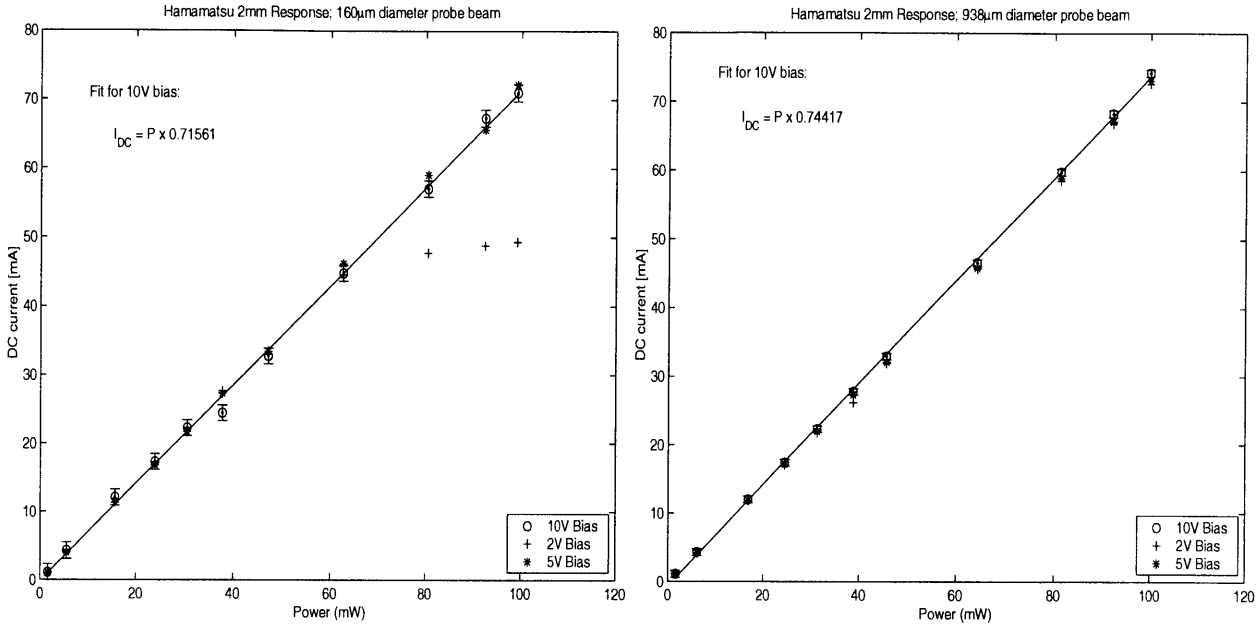

Figure 2.4: DC response of the 2mm Hamamatsu diode for two beam sizes

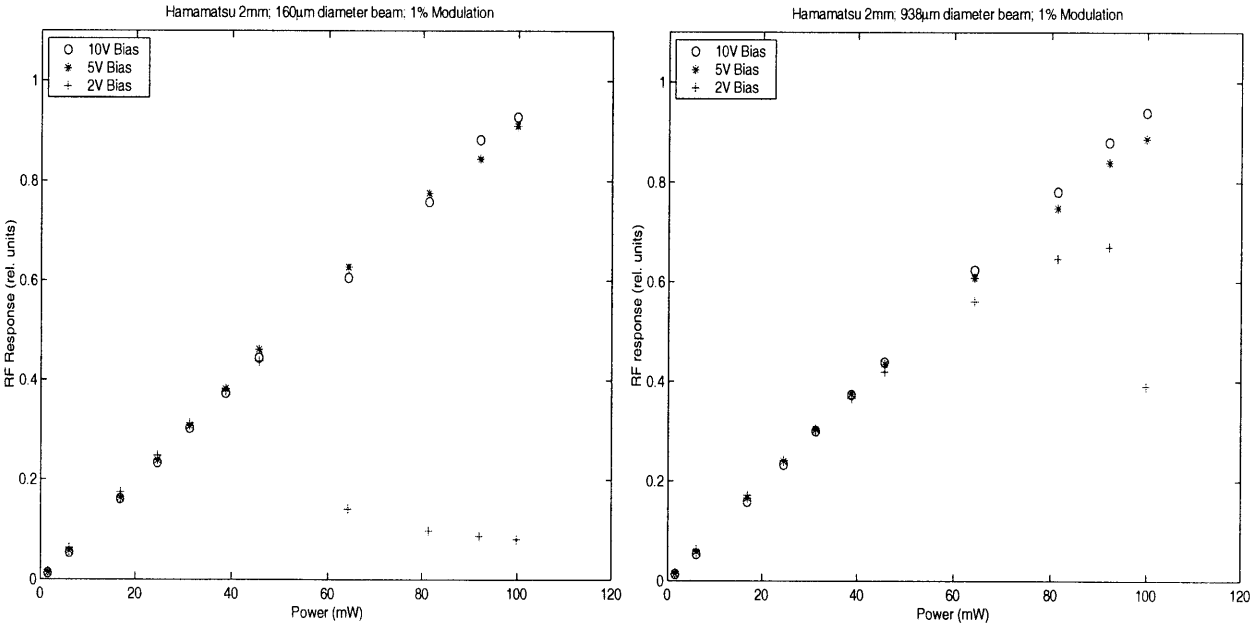

Figure 2.5: RF response of the 2mm Hamamatsu diode for two beam sizes

used and the vertical scale is arbitrary since it depends on the resonant impedance and the gain of the following amplifier. The EG&G diodes behave similarly and we omitted testing them at the lower bias voltages of 2V and 5V.

2.2.4 Beam Size

Figures 2.4 and 2.5 also illustrate that the dependence of the DC and RF response on beam diameter for the Hamamatsu 2mm diode is weak for diameters between 0.15 mm and 1 mm given sufficient reverse bias. A saturation effect can be observed for much smaller beams, an effect attributable to greater carrier densities generated in the junction depletion region that develop electric potentials counteracting the bias. We assume the EG&G diodes behave similarly to the Hamamatsu ones and we do not think this effect will play a great role in our application.

2.2.5 Modulation Depth

Light at the LIGO dark port is expected to have an amplitude modulation of about 0.15%. We studied the effects of modulations of up to 10% and notice saturation of the detector response at lower power levels for higher modulation. All other tests of the device were made at modulations of 0.2% or less.

2.2.6 DC Response

The critical questions to answer in relation to the DC output of the photodetectors are how much power one can submit the diodes to, and how linear their response is. None of the manufacturers recommend their diodes be operated under more than 10mW of light, and typically they suggest lower reverse biases than we use. However, due to the demands of our application, we measured the DC response up to the maximum available power of the laser (700mW). For the Hamamatsu diode with a 10V reverse bias, we found good linearity up to 400mW, whereas the EG&G diode was irreversibly damaged at close to 200mW. (The VIRGO collaboration, using a customized version of the Hamamatsu diode found similar power handling properties. [Mours '98]). At 700mW, the Hamamatsu showed an increase in dark current by a factor of about 100, though the capacitance and serial resistance were unchanged. The breakdown was observed to be "soft" in the sense that the dark current decreased as the device cooled (we shall have more to say about thermal effects later). Figure 2.6 shows the DC response of the EG&G, GPD InGaAs and GPD Germanium diodes in comparison with that of the Hamamatsu (all 2mm diameter). For incident powers up to 200mW, the response of the InGaAs diodes are essentially equivalent. The Germanium diode clearly has lower quantum efficiency.

2.2.7 RF Response

The RF response of the diodes is perhaps more important than their DC performance. It is also more dependent on the circuit around the diode; for purposes of comparison, however, we can still use our test circuit. Figure 2.7. presents the RF response of the 2 mm diodes at 25 MHZ (to which the resonant circuit was tuned) and a modulation of 0.12%. The Hamamatsu and EG&G diodes perform similarly well up to 200mW, while both GPD diodes fare more poorly. Figure 2.8 plots the response against photocurrent to eliminate some of the uncertainty due to the power meter and reflectivities.

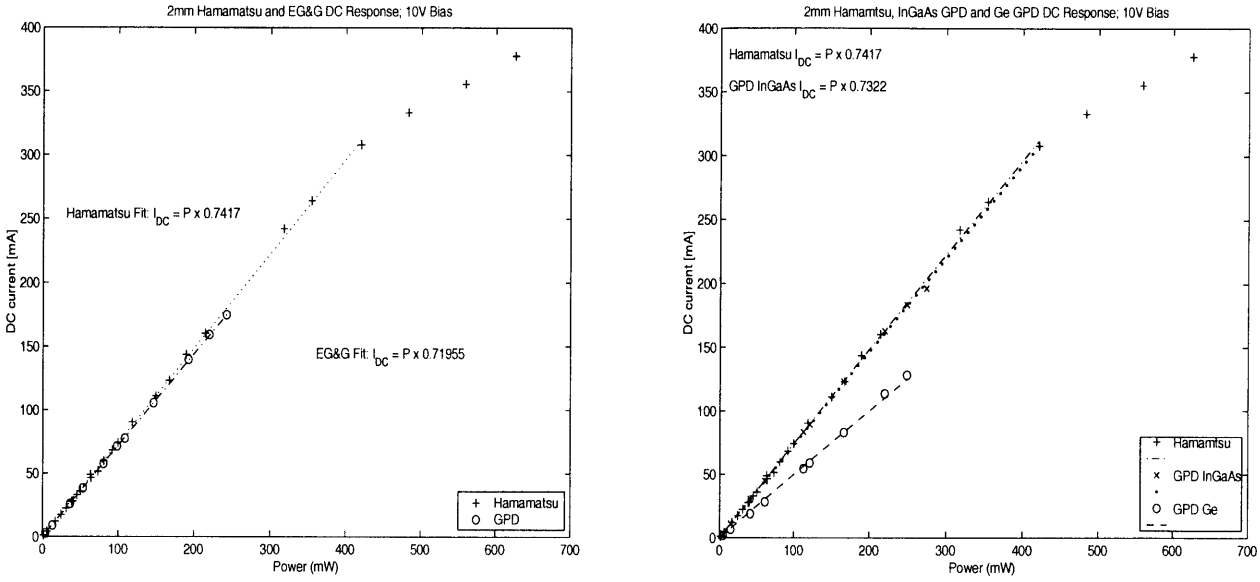

Figure 2.6: DC response of the EG&G and Hamamatsu (left) and the GPD and Hamamatsu (right) 2mm photodiodes.

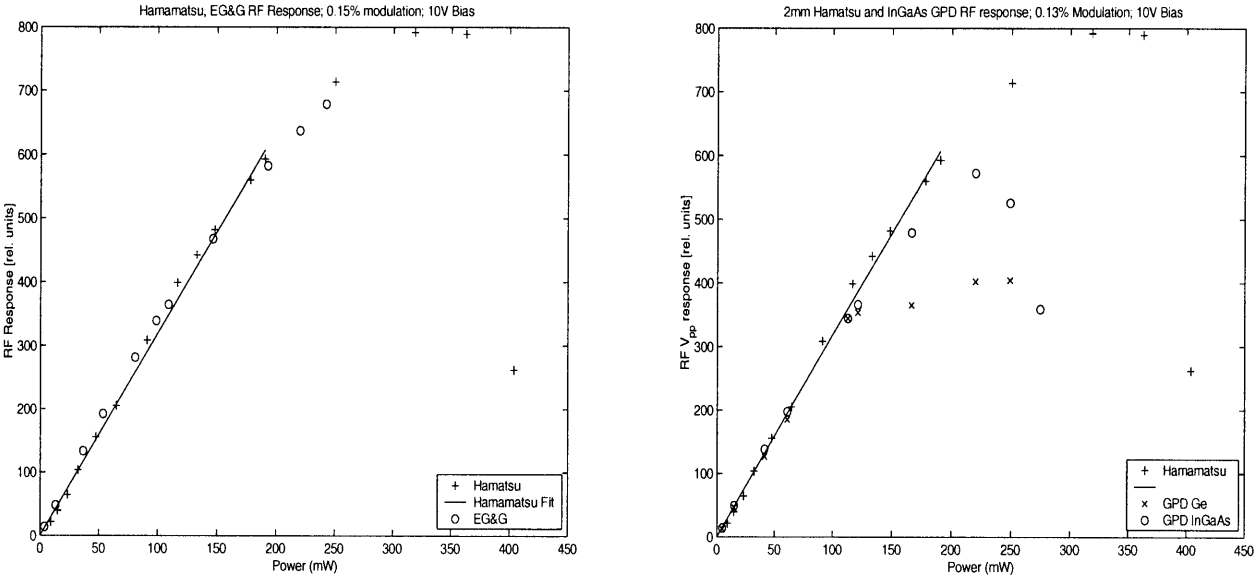

Figure 2.7: RF response of the EG&G and Hamamatsu (left) and the GPD and Hamamatsu (right) 2mm photodiodes. Some apparent gain compression at high powers is caused by lack of temperature compensation and by bias drop due to internal diode resistance.

2.2.8 Maximum Continuous Power Capability

To determine the number of photodetectors that will be needed to handle the continuous 600mW of power at the dark port, we subject the diodes to long duration tests (days to weeks) at relatively high powers and monitor the dark current, DC output and RF response. With ventilation and heatsinking, the Hamamatsu 2mm diode did not show performance degradation under

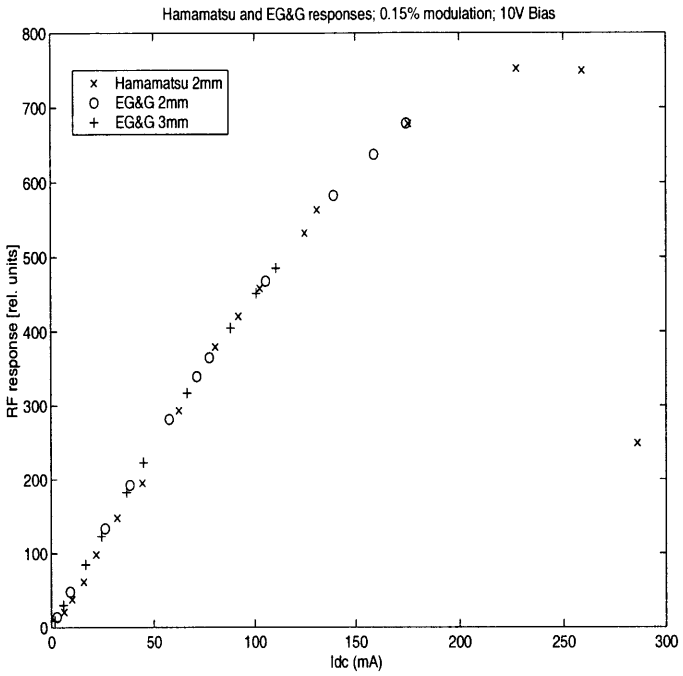

Figure 2.8: RF Response of the 2mm Hamamatsu and EG&G diodes as a function of generated photocurrent.

270mW of power and the EG&G under 200mW. We are therefore confident that four detectors at the LIGO dark port, each handling 150 mW, will be adequate.

2.2.9 Transient Peak Power Handling

An important consideration for photodetector operation while running the LIGO interferometer is what happens when the cavities fall out of lock due to a disturbance that the servo systems cannot track. Typically one expects that the energy circulating in the cavity falling out of lock is "dumped" onto the diodes on the time scale of the storage time of the cavity. For the arm cavities this would be approximately 3J in about 10ms, or an average power of 300W. Other transients can happen if the full input laser power (6 to 10W) is directed onto the diodes, happening on even faster time scales [LSC FDD]. The actual waveform of a transient is highly dependent on the disturbance and the nonlinear reactions of the servos; models for these exist, but realistically, we will have to gain experience through actual operation of the interferometer. Until then, we approximate the transient as a square-pulse, investigate thermal heating in the diodes (section 2.6) and rely on lower power tests. We know from preliminary tests that the Hamamatsu 2mm diode, without proper heatsinking, exhibited an increase in dark current when illuminated with 700mW under a reverse bias of 10V, and the EG&G diodes are tested by the manufacturer for 16 hours at 200C (although an EG&G device was damaged under approximately 280mW with reverse bias applied and no heatsinking). However, none of these conditions are representative of actual operating ones: the current design provides for excellent heatsinking of the diode case and the electronics include a current limiter to reduce electrical dissipation. Most importantly, the interferometer will

initially have very fast electro-optic shutters that should completely prevent catastrophic diode failure [LSC FDD].

2.3 Optical Properties

2.3.1 Reflectivity

We measure the reflectivity of the photodiodes under s- and p-polarized light. All the diodes have anti-reflection (AR) coatings and their windows are removed. Reflectivity is an important property because it can effect external quantum efficiency and is a source of stray light in the interferometer. In no case is there any advantage to having a more reflective diode.

We use a Stanford Research Systems SR810 DSP lock-in amplifier for a lock-in detection method (figure 2.9). The power input of the Lightwave 126-1064-700 laser is used for amplitude modulation and our detector is a commercial large area photodiode with an aluminum integrating sphere. (The diode was originally part of a Newport Research Corporation 815 power meter, and is used here as shown in figure A.4). The laser beam is focused down to a diameter of approximately 300μm at the diode under test (the exact value depends somewhat on laser power). The incident power is measured with the same integrating sphere detector before and after the measurements.

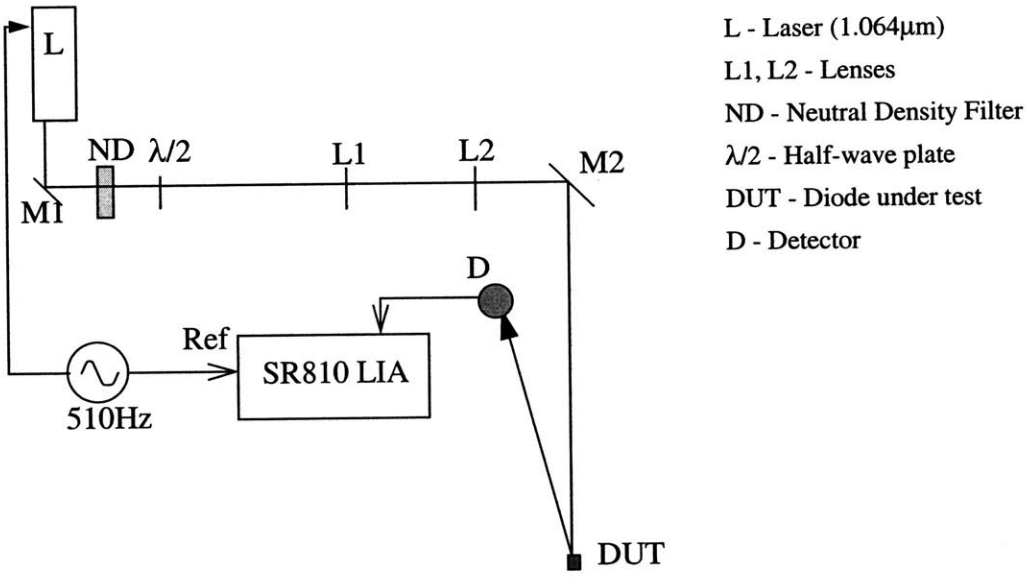

Figure 2.9: Reflection measurement setup.

The measured reflectivities are presented below in figures 2.10, 2.11, and 2.12. Surprisingly not all AR coatings achieve the same degree of impedance matching in coupling optical power from air to the diode. The Hamamatsu is the best of this group, although another factor of ten improvement should be possible [Byer '98]. (The difference in s- and p-polarization reflectivities for the Hamamatsu diode at near normal incidence is likely due to systematics in the instrumentation).

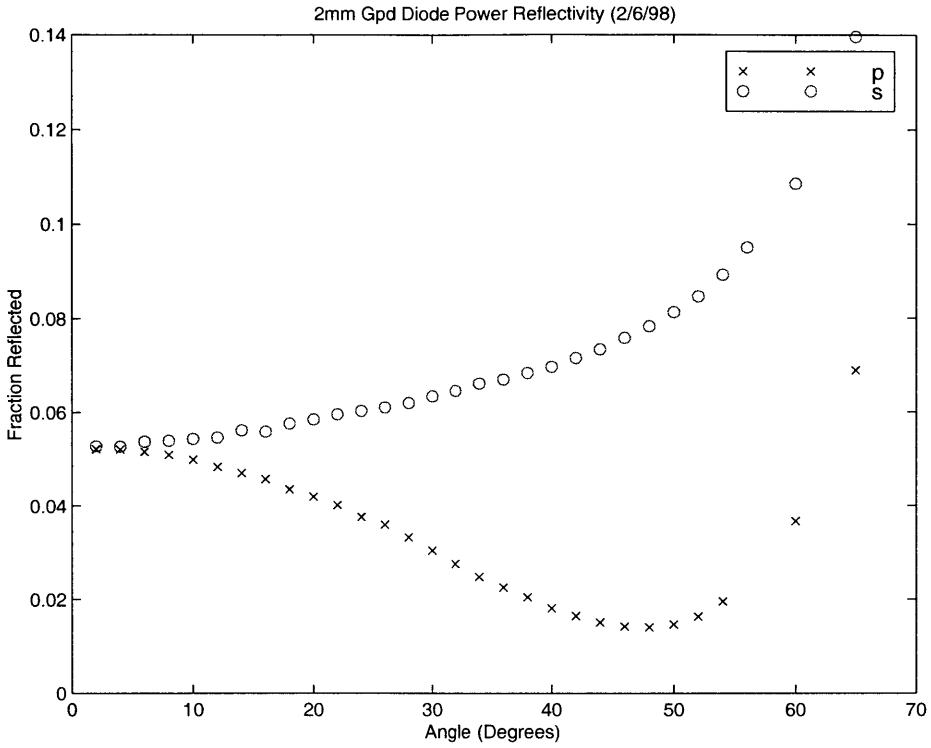

Figure 2.10: GPD Diode Reflectivity

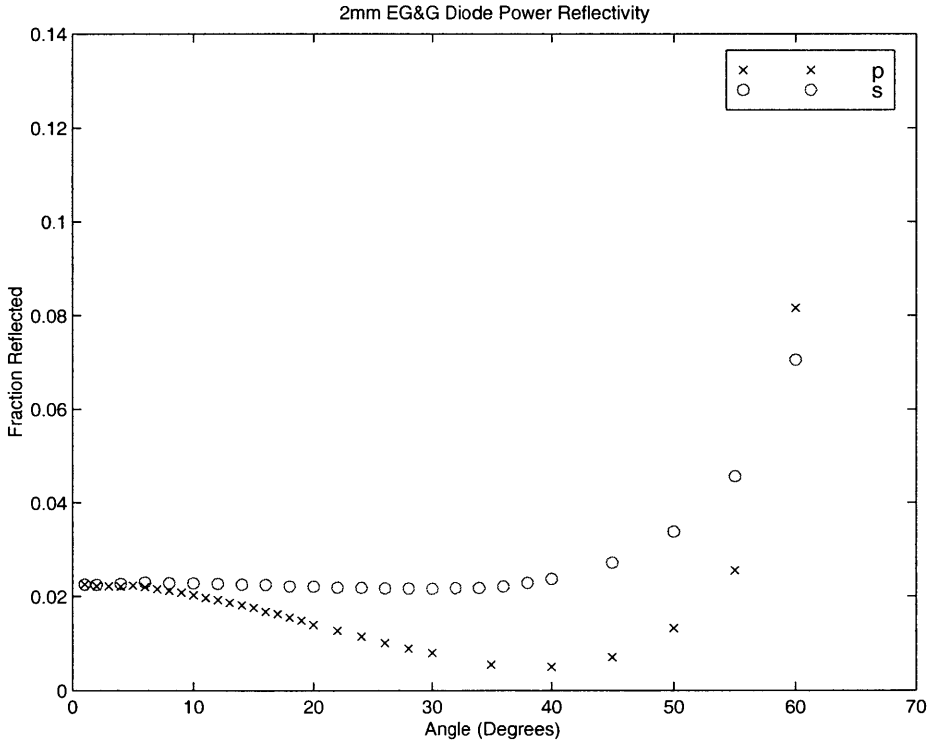

Figure 2.11: EG&G Diode Reflectivity

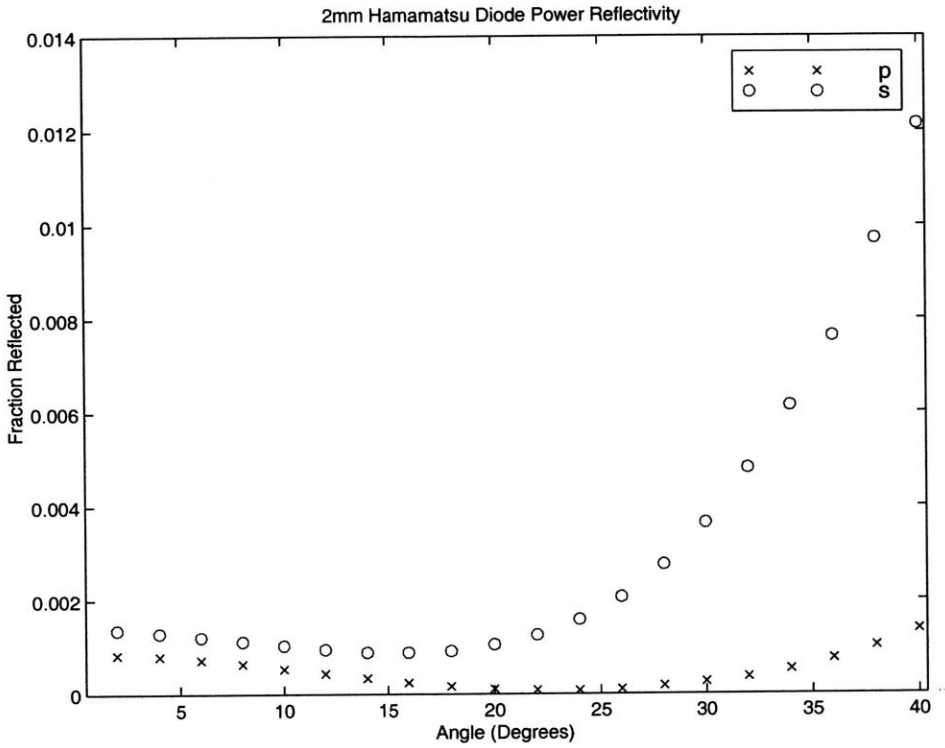

Figure 2.12: Hamamatsu Diode Reflectivity.

2.4 Backscatter

The Bidirectional Reflectance Distribution Function (BRDF) is a measure of the amount of light scattered from a target into a solid angle as a function of scattering angle and incident angle. There are various definitions in use for this quantity; we define the angles as in figure 2.13 and the

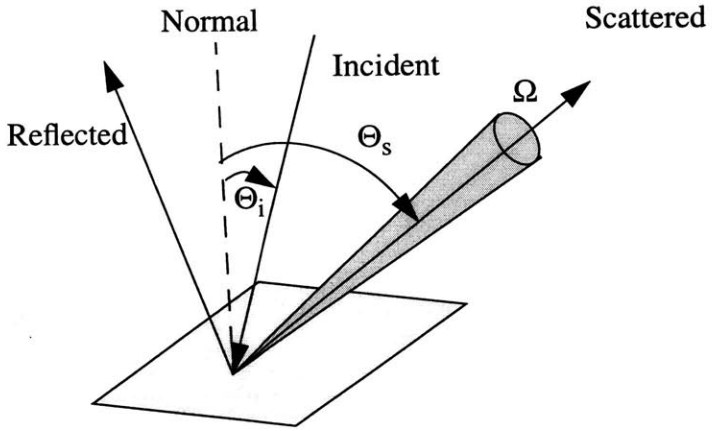

Figure 2.13: Definition of BRDF angles used in this document.

BRDF as

$$BRDF(\Theta_i, \Theta_s) \equiv \frac{P_{out}}{P_{in}\Omega} \tag{2.1}$$

where P_{out} is the scattered power, Ω is the solid angle and P_{in} is the incident power. This is referred to as the "cosine corrected" BRDF (traditionally, the definition of BRDF also includes a factor of the cosine of the scattering angle in the denominator).

2.4.1 Backscatter in LIGO

Although all detectors will be tilted slightly so that no light is specularly reflected into the interferometer, one still has to be concerned about backscatter from the photodiodes (Figure 2.14). Any light entering from the dark port will result in increased phase noise. Secondary scatter

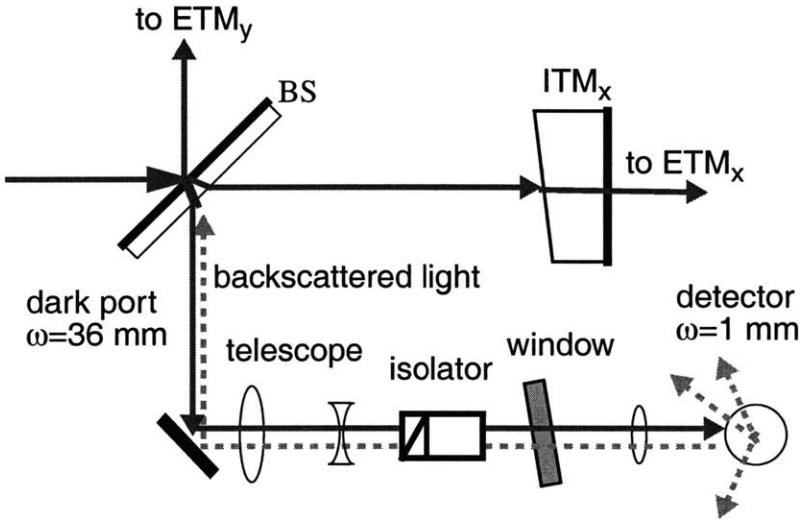

Figure 2.14: Backscatter path from the antisymmetric port photodiodes.

from the specularly reflected beams (about 2% of the incident power for the EG&G diodes that we plan to use, figure 2.11) will be insignificant once these beams are absorbed in beamdumps. The equivalent strain noise produced by the backscattered light is dependent on the power in the scattered beam, the magnification (ratio of beam waists at the beamsplitter and the photodiode), the solid angle of the beam in the interferometer, and the spectral density of motion of the scattering surface in the direction along the beam [LSC DRD]:

$$h_n^2(f) \sim P_{dp} \cdot BRDF(\Theta) \cdot \Delta\Omega \cdot \frac{\omega_0^2}{\omega_{pd}^2} \cdot \mathbf{x}_{pd}(f) \tag{2.2}$$

The diode motion is dependent on seismic and isolation conditions, and the BRDF on the smoothness of the diode surface. Neither is easily controllable. One could also reduce backscatter by lowering the magnification factor using a larger diode; however, we have found the 3mm diodes to be inadequate in nonuniformity and high junction capacitance. Using an optical isolator could reduce backscatter because its optical surface (which now becomes the relevant scattering surface) would

intersect the beam at a larger diameter, reducing the magnification factor; the disadvantage of using one is that it is yet another lossy element.

2.4.2 BRDF Measurements

We measure the BRDF of the surfaces using a technique similar to that for the reflectivity measurements. The setup is the same as in Figure 2.9, but we do not use the half-wave plate (the polarization of the light exiting the laser is vertical; this makes the incidence on the photodiode s-polarized). The detector assembly is made of a lens that images the scattered light onto a detection diode, baffling that extends from the lens part way to the detector, an iris that acts as a field stop, and a narrow band YAG-wavelength interference filter (figure 2.15). The detection diode is also

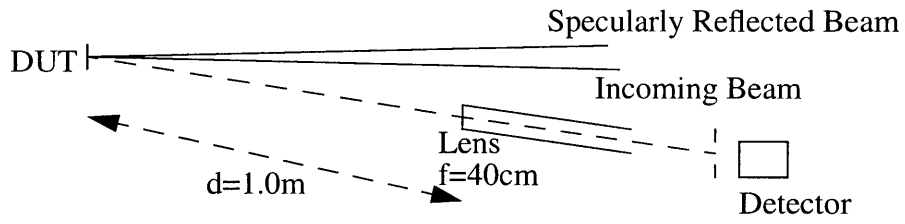

Figure 2.15: Scattered light detection setup.

an InGaAs device, its circuit is diagrammed in figure A.5. The iris is necessary because the incident beam is not perfectly clean and there is light falling on highly scattering regions of the packaging that are outside the diode (figure 2.16). We use a CCD camera to position the iris such that this parasitic scattering is eliminated, then swap the camera for the detection diode. The lens is placed as close to the incoming beam as possible to approximate direct backscatter; the angle relative to the incident beam is 4°.

2.4.3 Results

Table 2.1 lists the measured the BRDF of the diodes with an incident angle of 2.5° and a scattering angle of 6.5°. The LIGO requirement is that the ratio of phase-noise due to scattered light,

Table 2.1: 2mm Diode Backscatter

Diode	BRDF at 6.5° (10^{-4}/ster)
Hamamatsu (G5832-2)	1.1
EG&G (C30642G)	0.37
GPD (GAP2000)	0.11

to that due to other sources, be less than 0.1 [LSC DRD]. This translates to

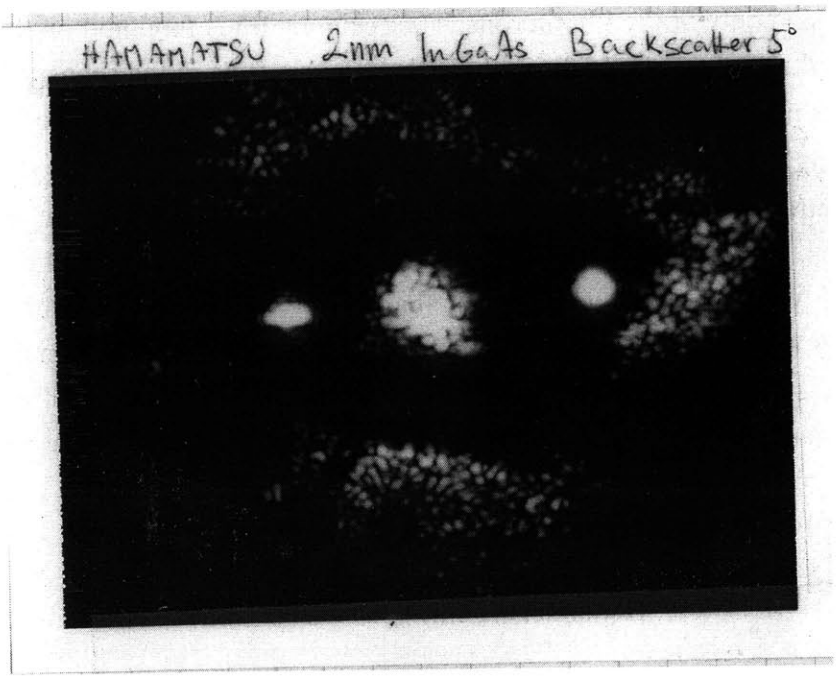

Figure 2.16: Image taken of the Hamamatsu 2mm diode surface through the same aperture that the backscatter was measured. The edges are bright due to the highly scattering material the diode is embedded on, despite the fact that less than 1% of the power is falling on that region.

$$x_{sc} \cdot m \cdot \sqrt{\text{BRDF}} \leq (2.4\times10^{-11}\text{m-ster}^{-1/2}/\sqrt{\text{Hz}}) \tag{2.3}$$

A conservative estimate for the diode motion of $10^{-11} m/\sqrt{Hz}$ for $f > 200$ Hz, a (de)magnification factor of 100, and the above BRDF values give

$$x_{sc} \cdot m \cdot \sqrt{\text{BRDF}} \cong 6\times10^{-12}\text{m-ster}^{-1/2}/\sqrt{\text{Hz}} \tag{2.4}$$

meeting the requirements by about a factor of four. We caution, however, that the BRDF can be sharply enhanced in direct retroreflection in comparison to the scatter at even very small angles, as we have measured [Stover '95].

2.5 Microroughness

In principle, one can use surface profile measurements to predict the optical scattering from surfaces, and vice-versa (ex. [Deumié '96]). To this end, we scanned the diodes with an atomic force microscope (AFM), Digital Instruments model Dimension 3000. The RMS surface height variation should predict the total integrated scatter, and spatial power spectra should determine the BRDF.

We took three square scans of relatively dust and defect free areas for one sample of each type of diode, of dimensions 1 by 1, 10 by 10, and 100 by 100 microns. The scans are all 512 by 512 pixels, except for the Hamamatsu 1 by 1 micron, which is 256 by 256 pixels. The 100 micrometer travel is near the limit of linear travel of the instrument, and when scanning the GPD diode, we

were able to manage only 90 by 90 microns. The scanning tip is mounted on a cylindrical piezoelectric element, the flexure of which produces bowing artifacts in the scans, therefore flattening post-processing is needed, especially for large tip displacements (large scanned areas).

We calculated one dimensional power spectra of the surface roughness by averaging the one dimensional spectra taken along each row and column of the digitized scan. In the case of the Hamamatsu scans, when the antireflective coating is taken into account, the model we use to derive the BRDF yields a result much lower than optically measured. In the case of the GPD diodes, the power spectra calculated from images of different size do not match at overlapping spatial scales; we suspect this is due to the processing in the microscopy software. At this point we feel that the surface scans do not yield good quantitative BRDF information but we list the measured RMS surface roughness to give an idea of the relative smoothness of the diodes. There

Table 2.2: RMS Surface Roughness

Scan size	Hamamatsu (nm)	GPD (nm)	EG&G (nm)
1μm × 1μm	6.81	0.954	2.69
10μm × 10μm	6.71	0.88	2.76
100μm × 100μm	6.815	2.9	2.19

is at least agreement in ranking the diodes by surface roughness and optically measured scatter.

2.6 Thermal Properties

2.6.1 Temperature Dependence of Diode Impedance.

The center frequency of the tuned test circuit clearly changes when the diode is illuminated. Such detuning can lead to gain compression and phase changes in the output. To investigate the possibility of the detuning being due to thermal effects, we measure the RF capacitance and resistance of the diodes as a function of temperature by placing the diode on a hot plate. For two Hamamatsu diodes we used an HP4195A RF Network Analyzer with its impedance test kit and a reverse bias voltage of 10V. For the EG&G and GPD diodes, we placed the diode in series with an inductor of 68μH, applied a reverse bias of 9V, and measured the resonant frequency of the resulting circuit with the HP 4195A in Spectrum mode. An EG&G diode was remeasured with the HP test kit in the same manner as the Hamamatsu, but with 8V reverse bias (figures 2.17, 2.18, and 2.19).

The two Hamamatsu diodes showed significant sample to sample variation at room temperature but approached similar values at higher temperatures. The GPD and EG&G diodes, in comparison to the Hamamatsu, have much lower capacitances that vary less with temperature (both fractionally and in the absolute sense).

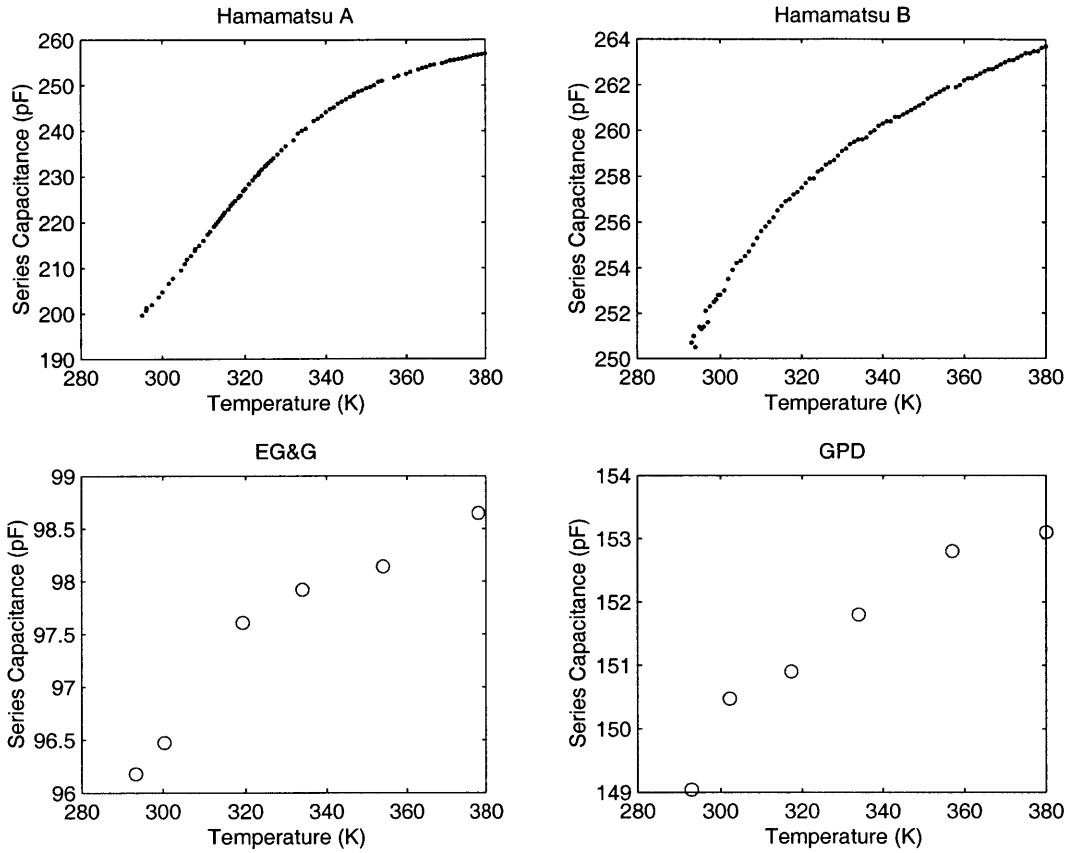

Figure 2.17: Temperature dependence of diode capacitances. Test jig capacitance of about 10pF was not subtracted for the EG&G and GPD plots.

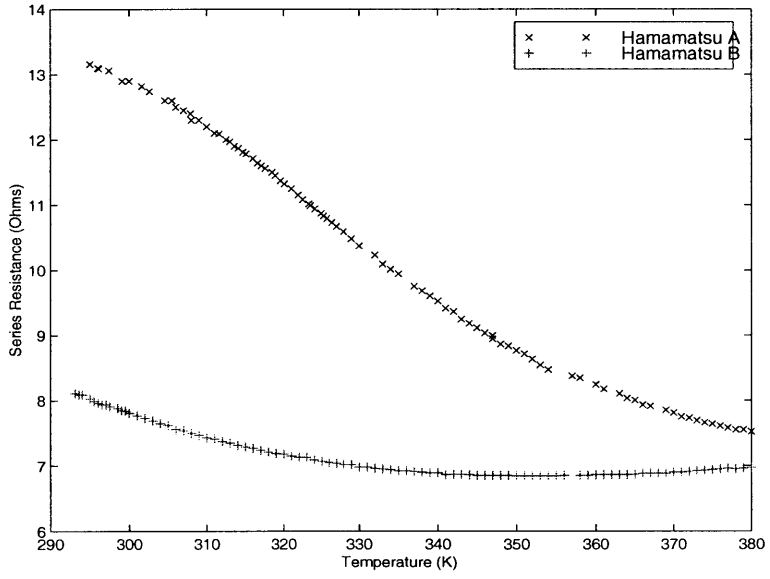

Figure 2.18: Temperature dependence of the series resistance of two Hamamatsu 2mm diodes. The two samples represent reasonably the upper and lower bounds of the range of typical diode resistances (at room temperature).

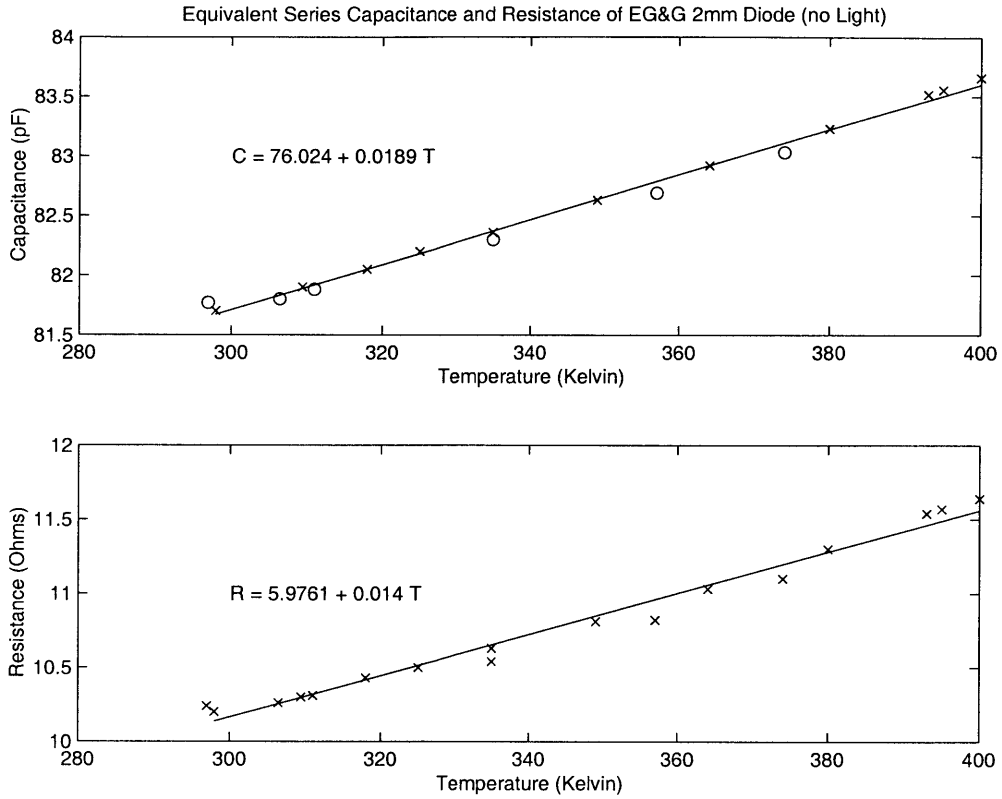

Figure 2.19: Temperature dependence of the capacitance and series resistance of the EG&G 2mm diode under 8V reverse bias.

The temperature dependence of the Hamamatsu and EG&G resistances were measured simultaneously with their capacitances (figures 2.18 and 2.19). The GPD diodes were not tested. As with the capacitance measurement, we find sample to sample variation in the resistance of the Hamamatsu diodes. The EG&G diodes, which are used in the final application, show less sample to sample variance, but even if this were to present itself as a source of problems in the interferometer, one can always resort to preselecting the diodes prior to installation in the detectors.

We now estimate the detuning. Based on the above measurements, the EG&G diode capacitance might change by about 1% under operating conditions of 15K above ambient (section 2.6.4). The measured resistance of roughly 10Ω leads to a drop in voltage across the diode, reducing the reverse bias, yielding an additional 4% change in capacitance (from the manufacturer's capacitance vs. bias voltage specifications). The two effects combine to change the phase of the RF signal by 7 degrees. The current circuit design compensates actively for the bias drop (figure A.2) and indeed, the phase changes by only about one degree (section 2.7).

2.6.2 Thermal Impedance

With reverse bias and about 150mW of light falling on a single photodiode, there is significant heating in the diode at the semiconductor junction due to optical absorption and electrical dissipation. This causes a substantial rise in the diode's operating temperature under steady-state conditions. Also, an interferometer unlocking event can dump large amounts of energy onto the diodes

on very short time scales, potentially causing device failure. We find the temperature increase by measuring the thermal impedance, the constant of proportionality between heat flow and the temperature gradient. We measure this parameter by using the diode itself as a thermometer, relying on the temperature dependence of the forward voltage drop across the junction.

2.6.3 Forward Voltage Drop

We describe how a PN junction diode can measure temperature. For an ideal p-n junction the current-voltage relationship is:

$$J = J_S(e^{qV_f/k_bT} - 1) \tag{2.5}$$

where V_f is the forward voltage, J_s is the reverse saturation current, q is the charge of an electron, and k_b is Boltzman's constant. For large enough forward bias, the exponential term dominates, so we may write

$$J = J_S(e^{qV_f/n_fk_BT}) \tag{2.6}$$

The above includes an ideality factor, n_f, that is traditionally used to account for non-ideal diode behavior, ohmic losses and generation and recombination effects at high and low at high current levels, respectively.

The reverse saturation current is

$$J_S = -qn_i^2\left(\frac{1}{N_D}\sqrt{\frac{D_h}{\tau_h}} + \frac{1}{N_A}\sqrt{\frac{D_e}{\tau_e}}\right) \tag{2.7}$$

where the D_h and D_e are diffusion coefficients, τ is the carrier lifetime, the labels h and e refer to holes and electrons, respectively; n_i is the intrinsic semiconductor carrier concentration, N_D and N_A are donor and acceptor concentrations and full ionization is assumed. The temperature dependence of n_i is $n_i \propto T^{3/2}e^{-E_g/2k_BT}$ and that of D/τ can be assumed to be T^γ, where γ is an integer [Bhattacharya '97]. This gives the temperature dependence of J_S:

$$J_S \propto T^{(3+\gamma/2)}e^{-E_g/k_BT} \tag{2.8}$$

Combining equations 2.6 and 2.8, the temperature dependence of the forward diode current is then

$$J \propto e^{qV_f/n_fk_BT}T^{(3+\gamma/2)}e^{-E_g/k_BT} \tag{2.9}$$

Note that the exponential terms will dominate the temperature behavior of the current, so if we keep the forward current, J, constant we then have

$$V_f \approx \frac{n_f}{q}(Ck_bT + E_g) \tag{2.10}$$

where C is some (negative) constant. We exploit the above relation, namely that the forward voltage is, to a good approximation, a linear function of temperature when the current flowing

through the diode is kept constant.

To measure the constant of proportionality between V_f and T, we pass a constant current in the forward direction through the p-i-n junction with no illumination and observe the voltage across the diode as we change its temperature. This gives us a calibration curve to use for the thermal impedance measurements. The diode is mounted on a copper plate which is heated with a resistor, and the temperature is read out by an Analog Devices model 590 sensor. The whole setup is insulated and placed in a box. For each data point, we manually change the resistor heating current and allow the temperature to stabilize. The results for the 2mm diodes tested are shown in figure 2.20. For all three types we obtain a forward voltage drop temperature coefficient of -2.1mV/K.

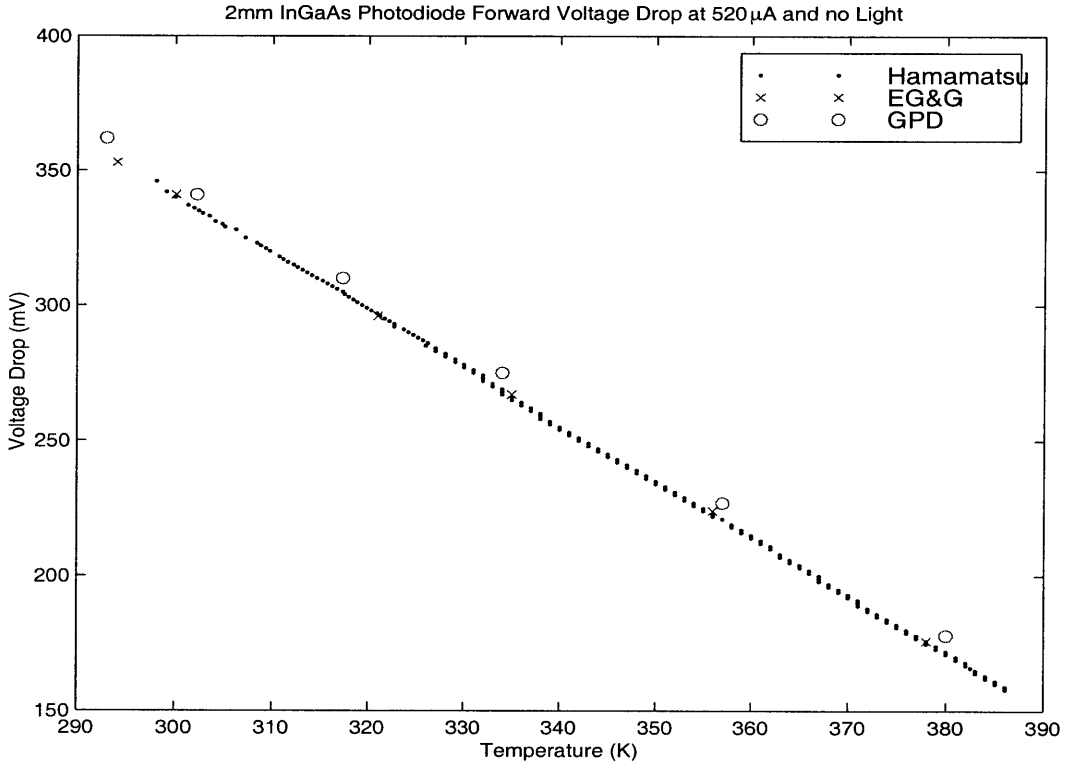

Figure 2.20: Calibration of the voltage drop vs. Temperature

The setup for measuring thermal impedance is shown in figures 2.21 and 2.22. (The circuit diagram for the current source is in figure A.3). The photodiode is mounted on a large heat sink to ensure that the case temperature does not rise by more than a Kelvin or so above ambient. (The thermal resistance of the heat sink is 1.3 K/W). The laser heats the diode surface and establishes a steady heat flow across the device. The forward voltage drop (V_f) decreases sharply with the absence of light when the laser is turned off, and then increases as the diode cools. (The value of V_f after the laser turn-off gives the thermal resistance from the junction to the ambient environment, which is dominated by the thermal resistance of the junction to case, Θ_{jc}). Figure 2.23 is the equivalent thermal circuit model, where C_j and C_c denote the heat capacity of the junction and case, respectively. The temperature response to laser power that is constant for $t < 0$ and is

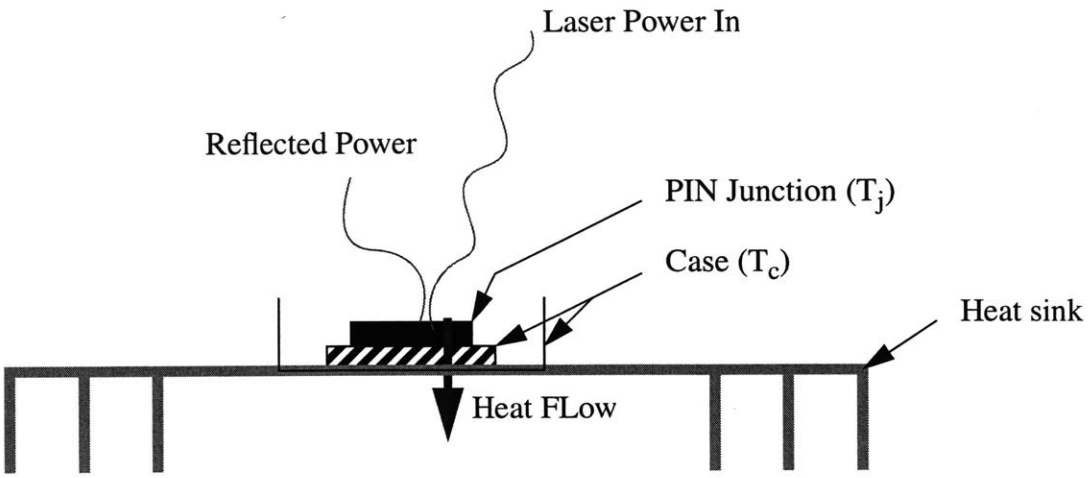

Figure 2.21: Schematic of Thermal Impedance measurement

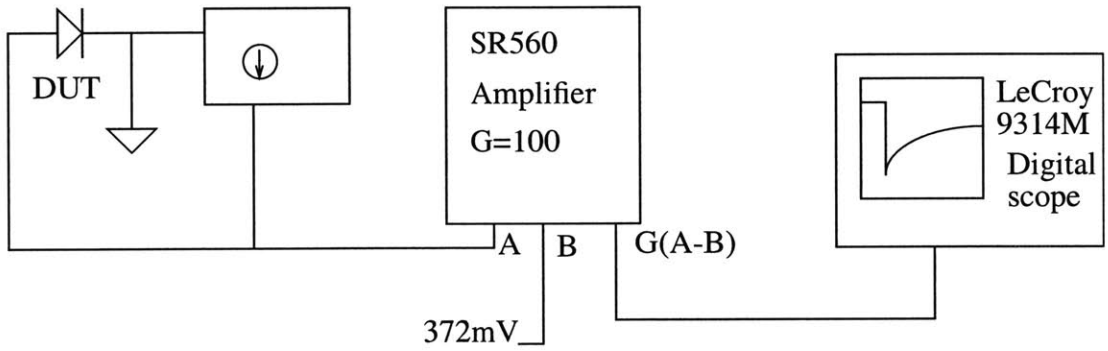

Figure 2.22: Setup for forward voltage drop measurements.

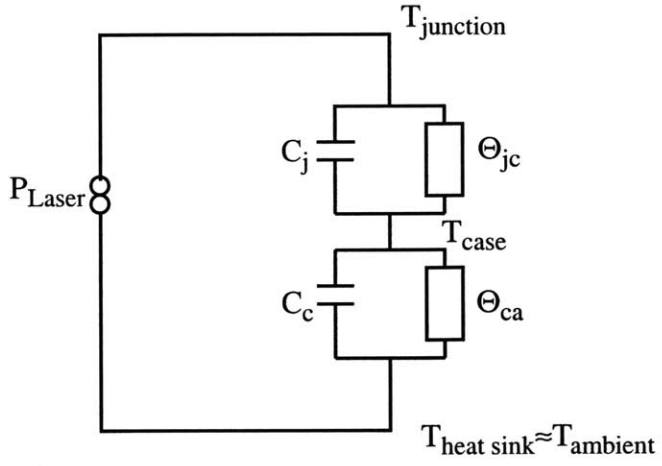

Figure 2.23: Equivalent circuit model for the thermal impedance measurement.

suddenly shut off at $t = 0$ is

$$T_j(t) = P_{Laser}\left[\Theta_{jc}e^{-\frac{t}{\Theta_{jc}C_j}} + \Theta_{ca}e^{-\frac{t}{\Theta_{ca}C_c}}\right] \tag{2.11}$$

2.6.4 Results

Figure 2.24 and 2.25 show the time dependence of V_f and the inferred junction temperature.

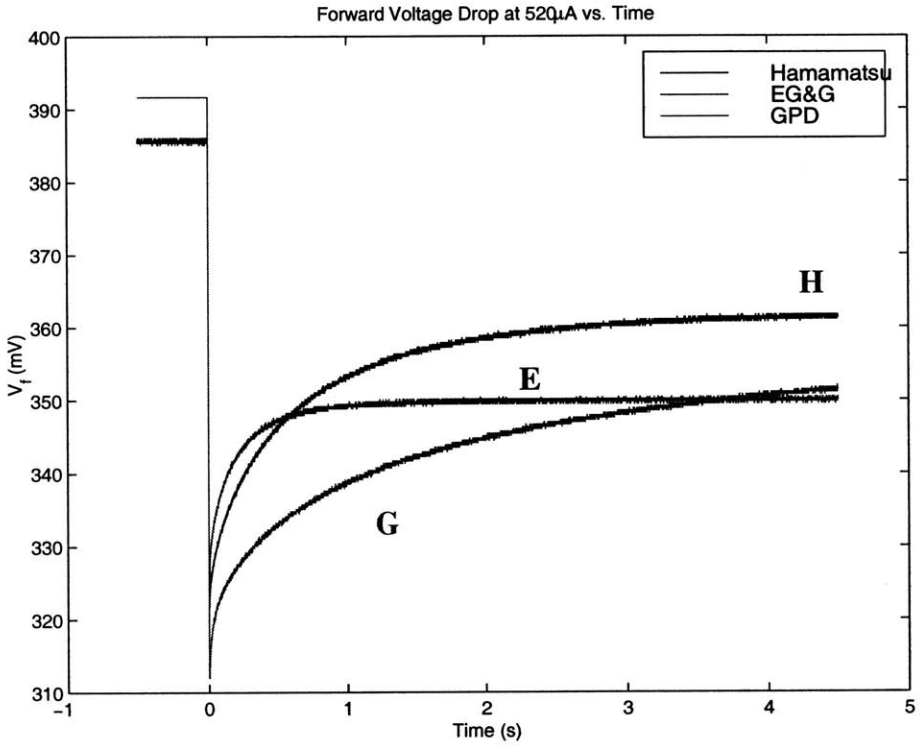

Figure 2.24: Forward Voltage Drop vs. Time. The origin of the time axis corresponds to turning the laser (and heating) off. Traces are labelled E, G, and H, corresponding to EG&G, GPD, and Hamamatsu.

To find the thermal impedances, we fit the nonlinear model of equation 2.11 to the temperature curve. The double exponential decay model that we derived is largely accurate; however, it cannot possibly account for all thermal processes, and indeed we find that a three (and even four) exponential decay model might fit the data better. We ignore the very long time scale decay, on the order of minutes, associated with the cooling of the heat sink. We also ignore, for the purposes of our fit, a decay lasting a few milliseconds at very beginning of the cooling process. This could be due any number of effects, including cooling of the bond wire, but is not the dominant contributor to the thermal resistance. With these considerations, we fit the data from 0.02 seconds after the laser turn off to the end of the data set using a nonlinear least squares fit. The physical constants extracted from the best fit parameters are in table 2.3. The errors are at least 3% due to our power meter. Uncertainties in the parameters estimated from $\Delta\chi^2$ are similar in size but the best fit

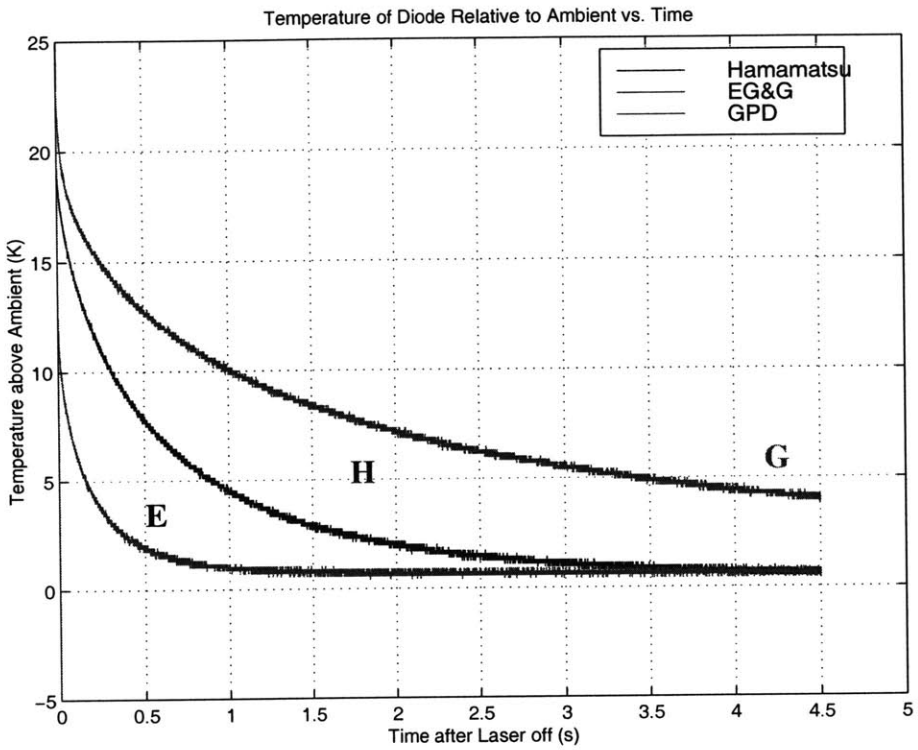

Figure 2.25: The data of figure 2.24 converted to Temperature. Traces are labelled E, G, and H, corresponding to EG&G, GPD, and Hamamatsu.

Table 2.3: 2mm Diode Thermal Impedances

Diode	Θ_{jc}(K/W)	C_j(J/K)	τ_j(s)	Θ_{ca}(K/W)	C_c(J/K)	τ_c(s)
EG&G (C30642G)	7.64	0.0172	0.13	5.04	0.0822	0.414
Hamamatsu (G5832-2)	8.44	0.027	0.23	14.0	0.0715	1.00
GPD (GAP2000)	6.47	0.0476	0.31	15.33	0.14	2.15

parameters depend sensitively on the offset constant of the fit. (We suggest that any future version of this experiment measure the heat sink or case temperature directly).

With this information we can now calculate the operating temperature of the EG&G diodes in the LIGO photodetector. Under steady state conditions, the bias voltage will be approximately 8V, the photocurrent 107mA, and the incident optical power 150mW, yielding a total power dissipation of just about 1W, and a temperature rise above ambient of $T_j = P(\Theta_{jc} + \Theta_{ca}) \approx 13K$. We may also assume an additional 2K for the temperature rise of the heat sink.

We can also calculate what happens in the case of an unlocking transient. The electrical power dissipation in the diode with the current limited to 200mA and a diode resistance of approximately 10Ω will be 0.40W. This is very small in comparison with optical power peaks up to 75W (the 300W transient divided onto four diodes, see section 2.2.9). Note however, that if we were

not to have the current limiter, the electrical power dissipation could exceed the optical power by a factor of 5 to 6, depending on the bias voltage. If we now assume that a total energy of E_{pulse} is incident on the diode and uniformly distributed in time T, the maximum junction temperature will be reached at the end of the pulse:

$$T_{max} = \frac{E_{pulse}}{T}\left[\Theta_{jc}\left(1 - \exp\left(-\frac{T}{\tau_j}\right)\right) + \Theta_{ca}\left(1 - \exp\left(-\frac{T}{\tau_c}\right)\right)\right] \tag{2.12}$$

For small times, where T is less than either time constant, time is too short for the heat to redistribute (for the EG&G, $T \ll 0.02s$) and the maximum temperature reduces to $T_{max} = E_{pulse}(1/C_j + 1/C_c)$. For the EG&G diode, this will result in a temperature rise of $70K/J$, or about 53C above ambient for the expected 3J interferometer transient (again, assuming four detectors). In this respect, the EG&G diode is the worst performer (figure 2.26).

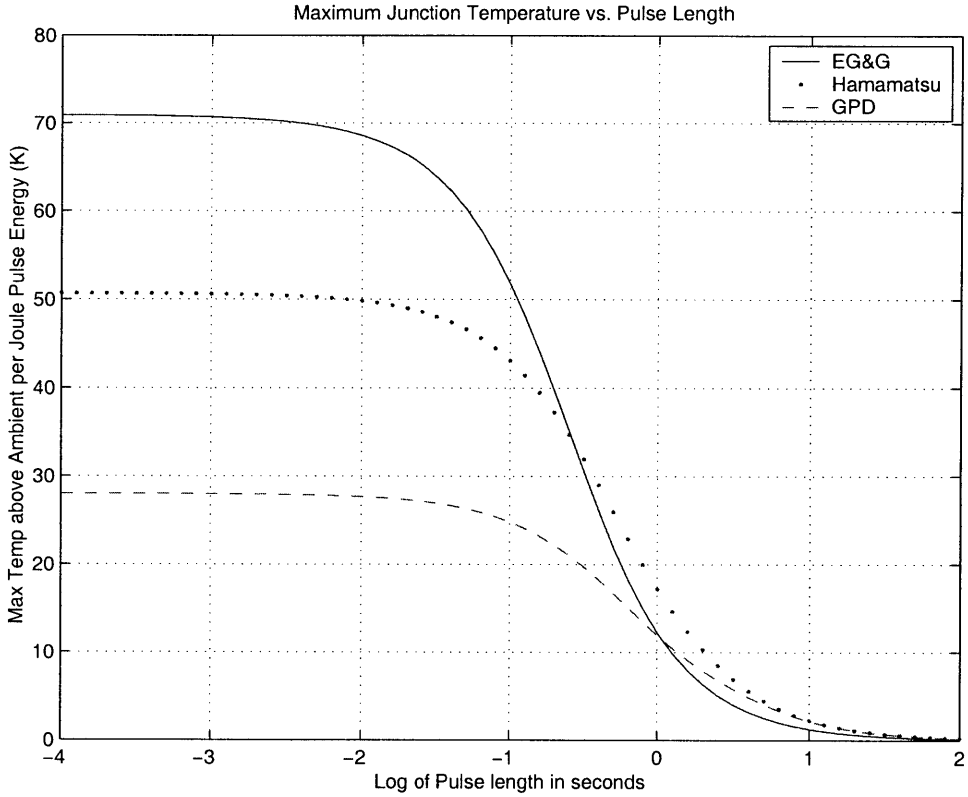

Figure 2.26: Calculated temperature response of the 2mm InGaAs diodes based on thermal impedance measurements and a double exponential thermal decay model.

2.7 Tests of the First Article

2.7.1 Resonant Impedance

We measured the resonant impedance of the first LIGO production model photodetector by using an incoherent light source to generate shot noise limited photocurrent. The DC output gives us the average photocurrent with the shot noise scaling as its square-root (see section 1.3). Subtracting

dark noise and dividing the RF output voltage power spectral density by the RF stage gain and the current power spectral density gives us the impedance. The measured values are listed in table 2.4.

DC Photocurrent (mA)	Z_R (Ω)
178	231
135	241
111	246
89	254
68	259
46	273
23	283

Table 2.4: Measured resonant impedance as function of photocurrent.

One would expect a constant impedance but the observed nonlinearity could be due to the active bias circuit that is designed to compensate for the ohmic losses in the diode at high photocurrents by raising the bias voltage.

We also tested the first article for heating and thermal effects. The unit has an integrated thermal sensor on the heat sink, so the reported temperature is not that of the junction. In any case, the relevant quantity to measure is the phase shift of the RF output signal as a function of detected power. We made a network measurement using the setup of figure 2.1 at various powers and find only a minimal phase dependence of $d\varphi/dP \approx (0.04)°/mW$ at 150mW (figure 2.27).

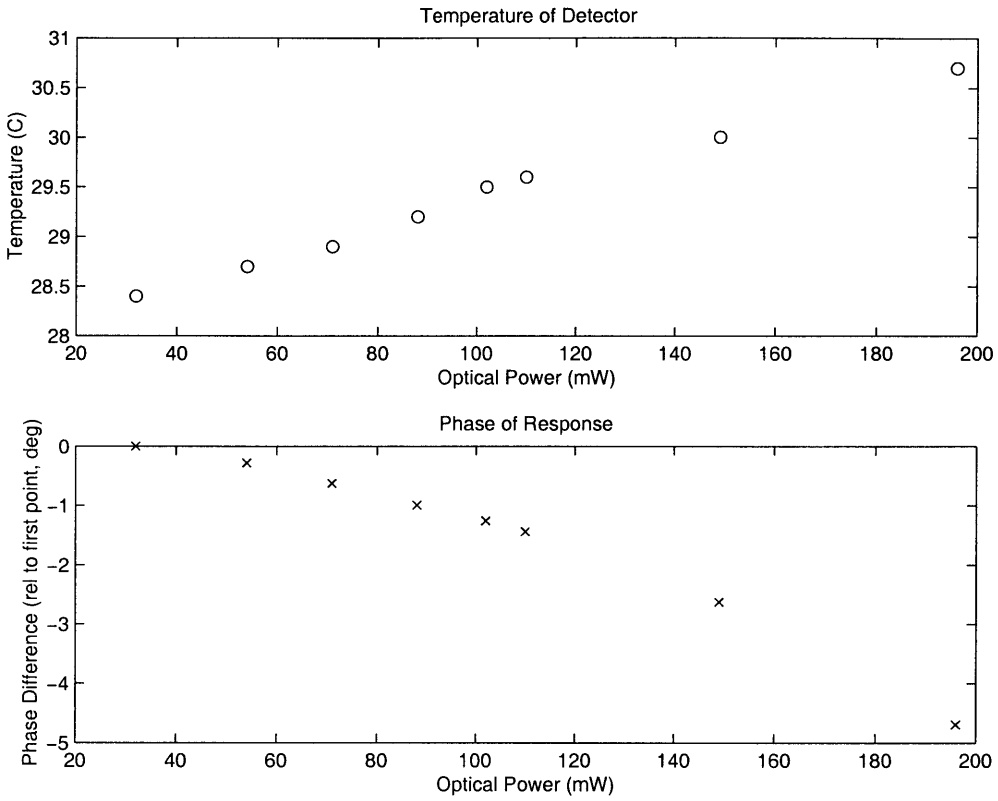

Figure 2.27: Change of RF signal phase as a function of average optical power for the LIGO dark port detectors (first article).

Chapter 3

Prestabilized Laser Intensity Noise

3.1 Introduction

We measured the intensity noise of the Hanford 2km interferometer prestabilized laser (PSL) in a frequency range of 100kHz to 100MHz. This was done on 15 Dec 1998 as part of the validation process for the subsystem. The requirements, as described in section 1.4, are specified in terms of the shot noise fluctuations of a 600mW beam; however our detector, which we describe in this chapter, is capable of measuring only a 142mW beam. We must therefore extrapolate our results to higher powers. Our measurements reveal that having the low frequency power servo (intensity servo, or ISS) after the PMC is likely the cause of excess noise and, more importantly, that the required noise level at the LSC modulation frequencies may not be met. We also compare the noise measured just before the pre-modecleaner (PMC) to that measured at the output of the PSL assembly and find the intensity filtering performance of the PMC.

3.2 The Broadband Detector

3.2.1 Design

We built a broadband detector whose design is based on the circuit developed for the LSC detectors at the dark port of LIGO. It uses the same diodes, and consequently would be able to handle the same amount of optical power were it not for a limitation imposed by the photocurrent (see below). Whereas the LSC design uses a tuned resonant circuit to increase gain at the appropriate frequencies (section 1.3), we aim for maximal bandwidth and thus remove the tuning inductor and the other reactive elements used for notch and bandstop filtering. Our circuit diagram is shown in figure 3.1 (All further component references will be for this diagram). It retains the key feature of the LSC design, the op-amp U2, which biases the photodiode D1 (EG&G 2mm InGaAs diode, model C30642G). The nominal bias level is augmented as a function of the photocurrent to compensate for the voltage drop due to the load resistance and the diode bulk resistance. Voltage reference U9 is configured to provide a nominal 7.02V, and op-amp U5 provides a feedback signal proportional to the photocurrent. The bias level is therefore $V_{Bias} = 7.02V + I_{phot} \cdot 62.2\Omega$ relative to ground.

The load resistance in series with the diode puts a limitation on the maximum current and vice-versa, since the op-amp U2 must be able to swing high enough in voltage. We found for operating at 100mA photocurrent, the positive supply had to be raised slightly to +16.5V. This is within the operating voltage range of all circuit components.

The DC current is read out through two op-amp stages, U5 and U6, giving a transimpedance gain of 22.7 Ohms into a high impedance.

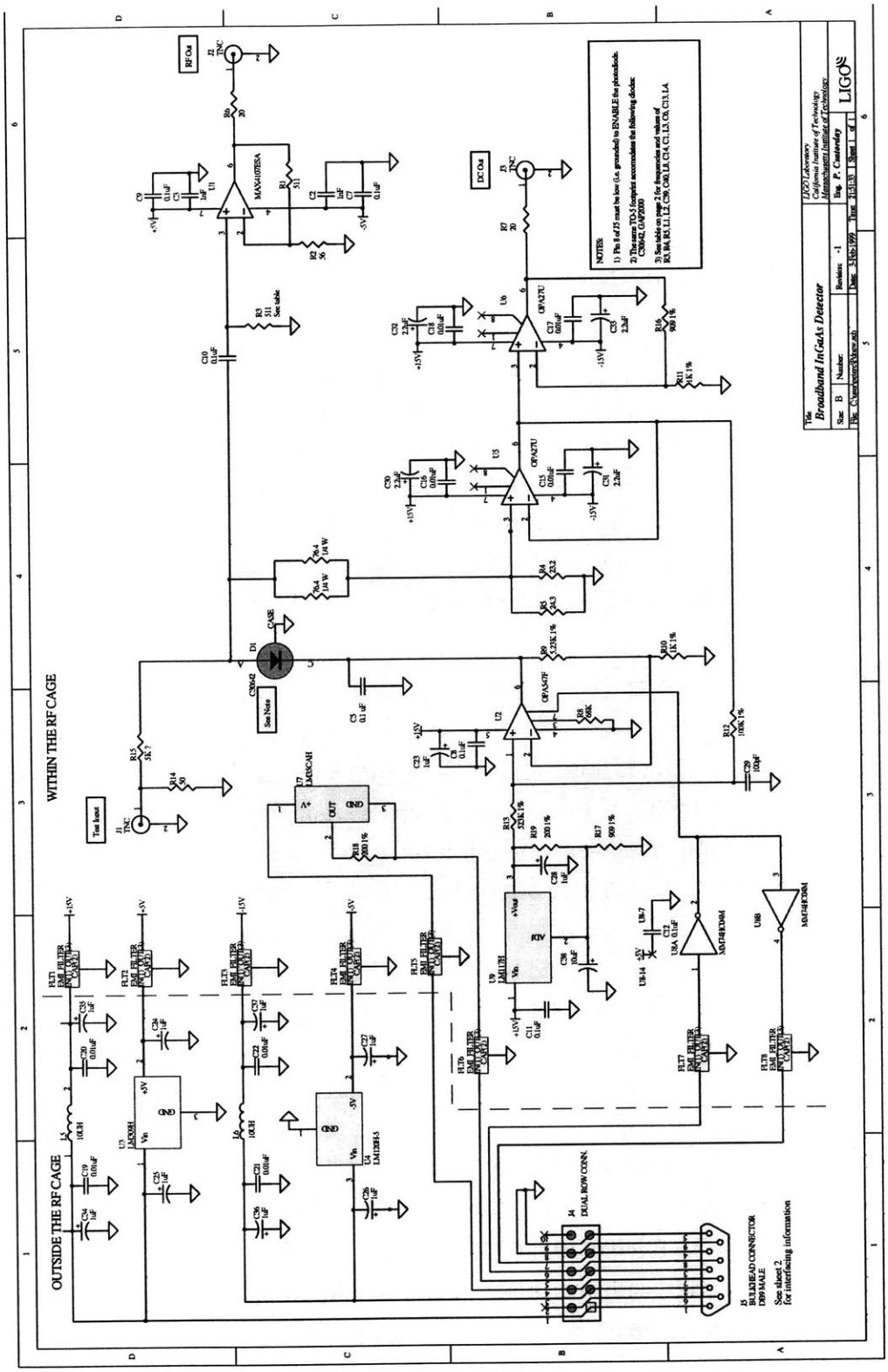

Figure 3.1: Broadband Detector Circuit Diagram

The RF output stage is a capacitively coupled MAX4107 op-amp in a transimpedance configuration. This device has a remarkably low $0.75nV/\sqrt{Hz}$ voltage noise above 10kHz, and a 300MHz bandwidth at a gain of 10. The input bias current limits our choice of R3 to 511Ω. A 0.1μF capacitor (C10) and R3 high-pass couple the RF stage and lower the load resistance to about 45.5Ω at frequencies above 3.1 kHz. With these values, we calculate an RF stage transimpedance of 330 Ω into a 50Ω line. This is borne out by measurements using a shot noise limited incandescent light source: the expected signal is $330\Omega\sqrt{2eI}$ which for 100mA of photocurrent is $5.9 \times 10^{-8} V/\sqrt{Hz}$, as measured (figure 3.9).

3.3 Detector Performance

Frequency Response

3.3.1 Optically Measured

We measure the frequency response of the detector using a current-modulated laser diode. The diode puts out 40mW of optical power, the impressed modulation is high-pass coupled at 30kHz which we independently measure to be flat within 1dB out to 100MHz. Based on these optical measurements, the -3dB bandwidth of our detector is 33 MHz (see figures 3.2 and 3.3).

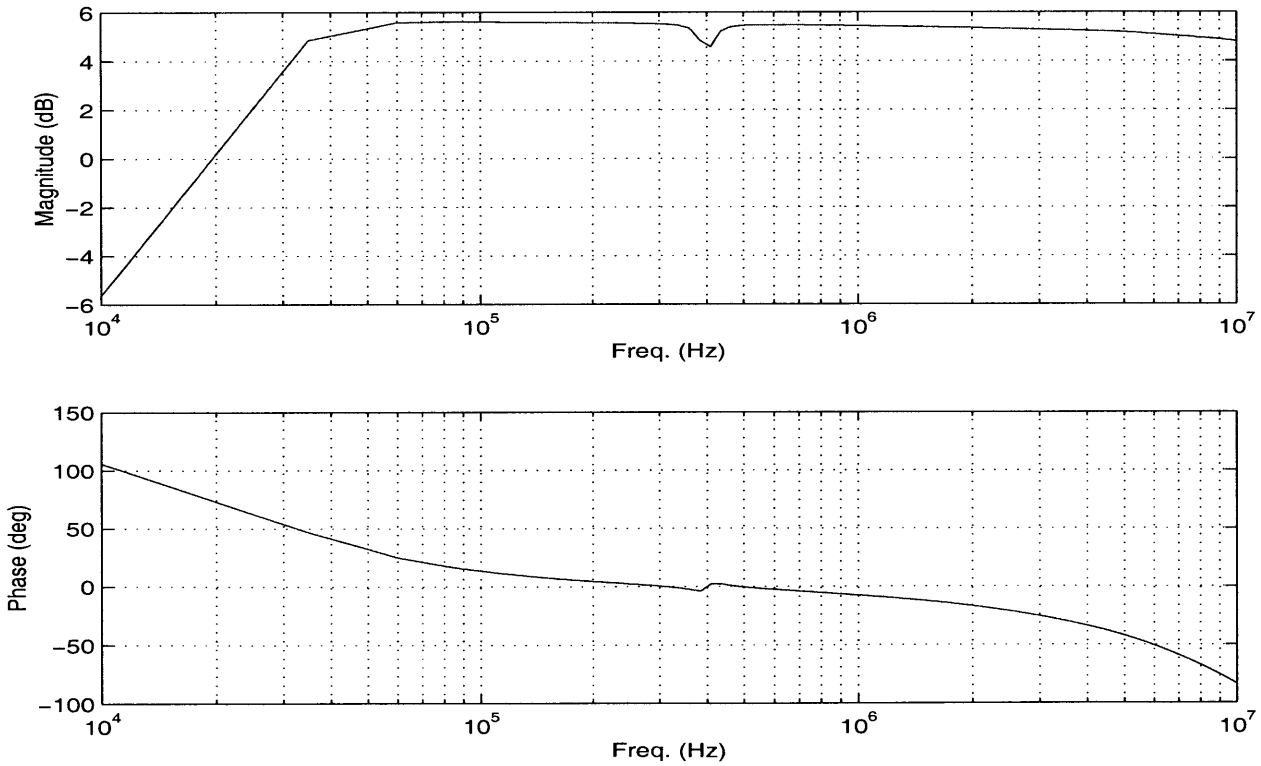

Figure 3.2: Optically measured broadband detector frequency response. (10kHz - 10MHz) There are two zeros at about 30kHz, one each in the modulation and detection circtuits.The small glitch at 400kHz is unexplained.

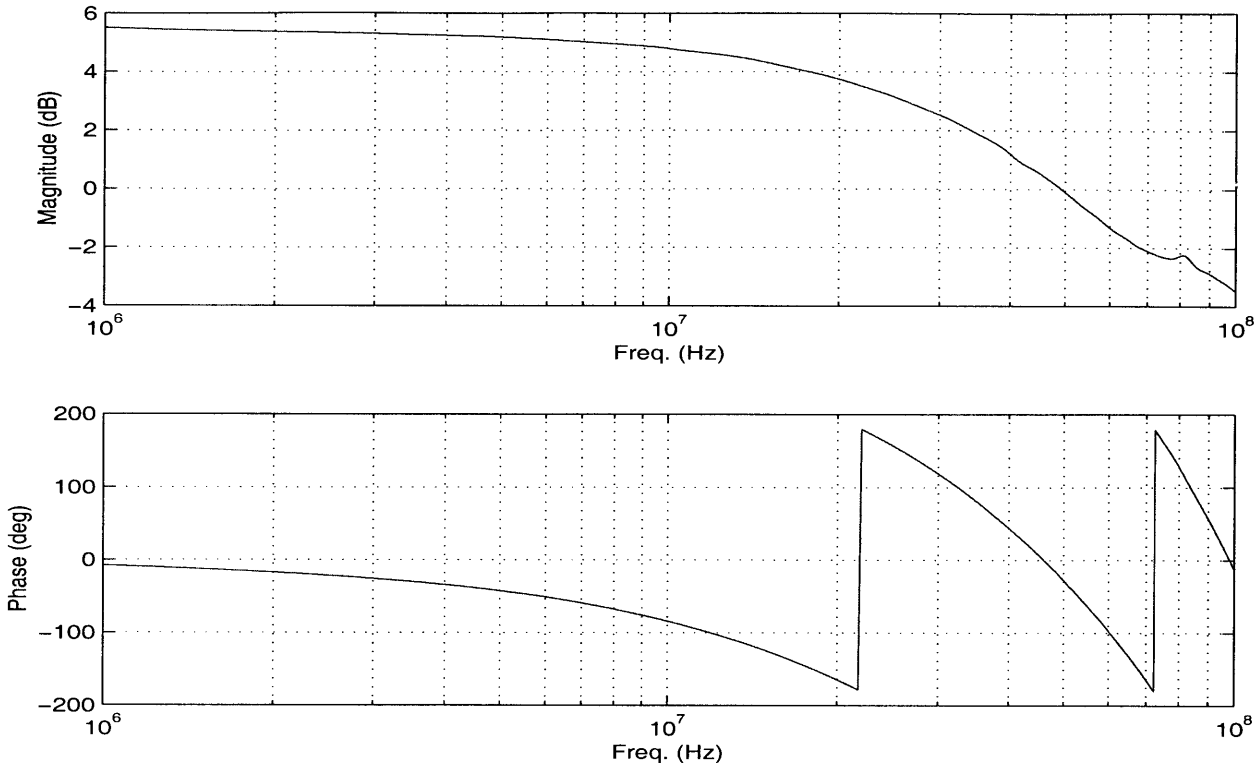

Figure 3.3: Optically measured broadband detector frequency response. (1MHz - 100MHz)

3.3.2 Electronically Measured

The LSC circuit design also provides for an electrical test input (J1). The transfer function measured through this input is shown in figures 3.4 and 3.5. The bandwidth obtained is the same as that from the optical measurements.

3.3.3 Noise Performance

We estimate the noise we expect due to the MAX4107 and from the resistors. The voltage and current noise figures for the chip above 10kHz are, according to specifications, $e_n = 0.75nV/\sqrt{Hz}$ and $i_n = 2.5pA/\sqrt{Hz}$. The parallel combination of feedback resistors gives a total resistance of $r_{FB} = 50.5\Omega$. The expected noise is approximately

$$V_n = \sqrt{e_n^2 + 4kT(R_{FB} + R_S) + i_n^2(R_{FB}^2 + R_S^2)} \tag{3.1}$$

where T is the temperature and R_S is the source resistance (physically the same quantity as the load resistance of section 3.2). Using 295K and 45.5Ω for these quantities, we find $V_n = 1.47nV/\sqrt{Hz}$, or $10.6nV/\sqrt{Hz}$ at the output, accounting for gain and assuming a 50Ω transmission line. The noise of the HP 4195A spectrum analyzer is measured to be about $7nV/\sqrt{Hz}$, so we expect to observe a dark noise level of $12.7nV/\sqrt{Hz}$. This is in good agreement with actual measured values (figure 3.6).

Based on the above calculation, the noise figure (NF) of the RF amplifier stage is:

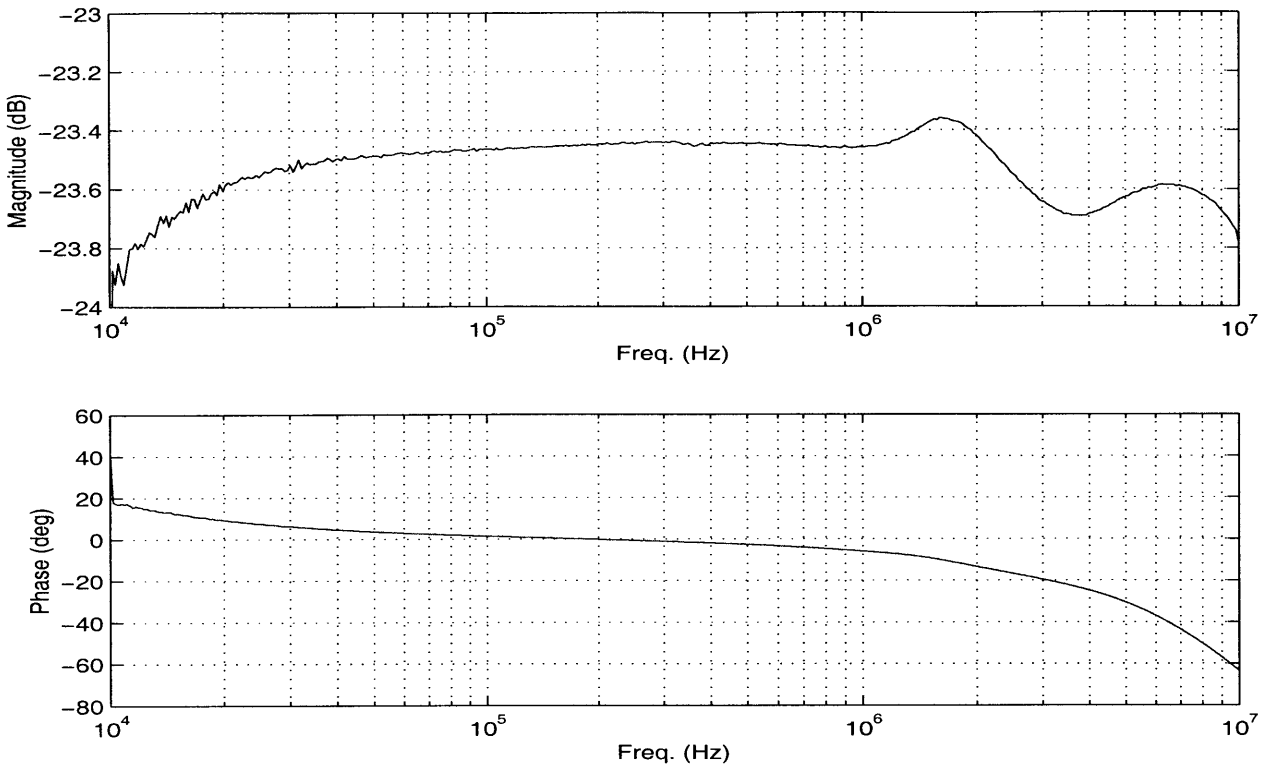

Figure 3.4: Electrically measured broadband detector frequency response. (10 kHz - 10 MHz) The 0.3 dB ripple near 2MHz is due to slightly overloading the analyzer input stage.

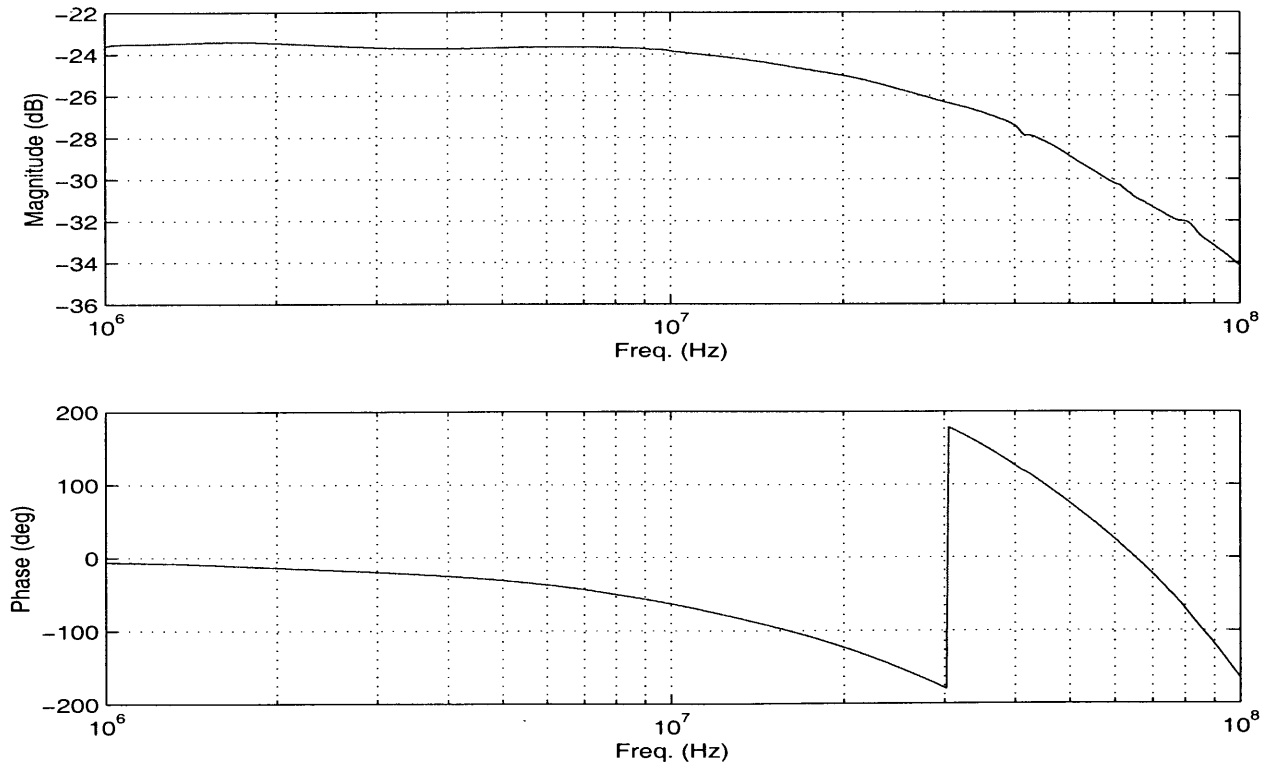

Figure 3.5: Electrically measured broadband detector frequency response. (1MHz - 100MHz)

$$NF = 10\log\left(1 + \frac{V_n^2}{4kTR_S}\right) = 10\log(1 + 2.92) = 5.9\text{dB} \tag{3.2}$$

Equivalently, the noise temperature is 590K.

Figure 3.6 shows the measured dark noise of the detector and the instrument noise (with the

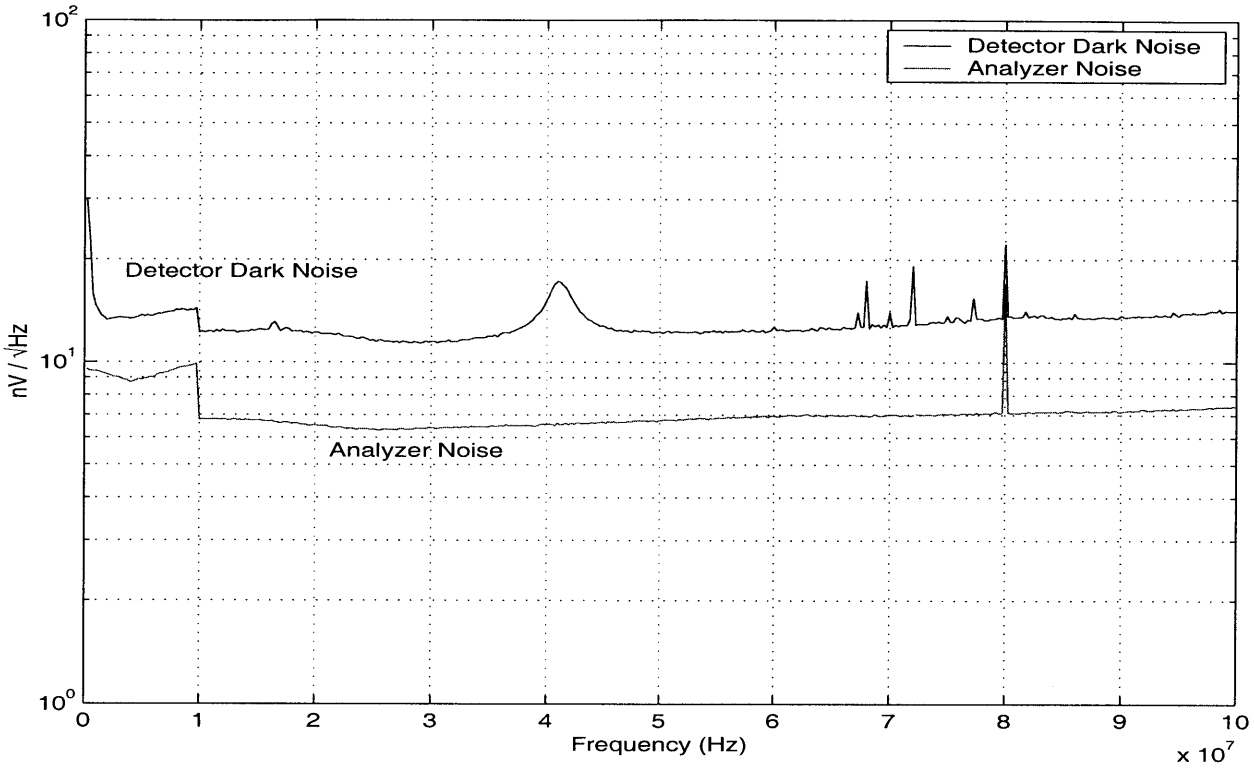

Figure 3.6: Broadband detector dark noise and analyzer noise.

4195A in high IF sensitivity mode and a 50Ω terminator with no attenuation at the input). The source of the broad peak around 41 MHz has not yet been identified; it appeared when a 5.6 nF capacitor in parallel with R4 and R5 was removed. That step was made to ensure that the load resistance was not being rolled off at higher frequencies. Other peaks in the spectrum correspond to TV and radio stations in the Cambridge, Massachusetts area, and were not present at Hanford, Washington. The 80 Mhz line in the analyzer noise is unexplained (perhaps due to the CRT refresh), as is the excess noise below 10 MHz and the sudden drop thereafter (this latter effect is consistently seen in the HP4195A which has an internal oscillator at 10MHz).

We need to compare the above measured detector noise to the signal level expected from a shot noise limited beam. To do this, we illuminate the detector with light from an incoherent source (an incandescent bulb). Figure 3.7 shows this comparison. Low frequencies are rolled off by a whitening filter in order not to saturate the input stage of the spectrum analyzer. We see that the noise equivalent power is at least 12 to 4 dB below our expected signal level, depending on frequency.

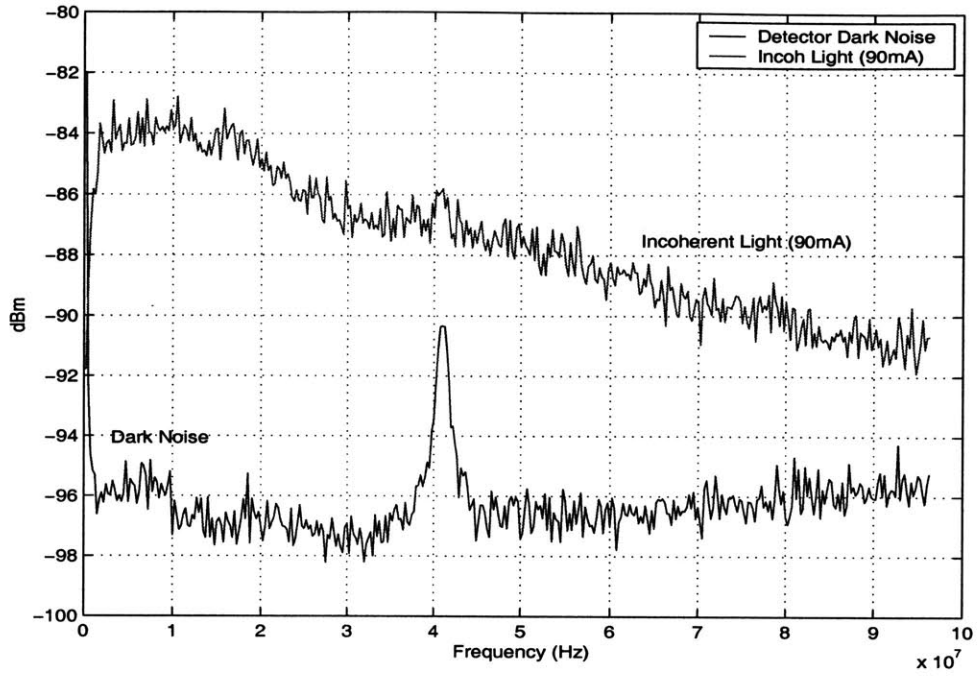

Figure 3.7: Shot noise test of the broadband detector. The peak around 4MHz is the same as that in figure 3.6.

3.4 PSL Intensity Noise Measurements

Figure 3.8 outlines the setup of the PSL during our measurements. All servo parameters were

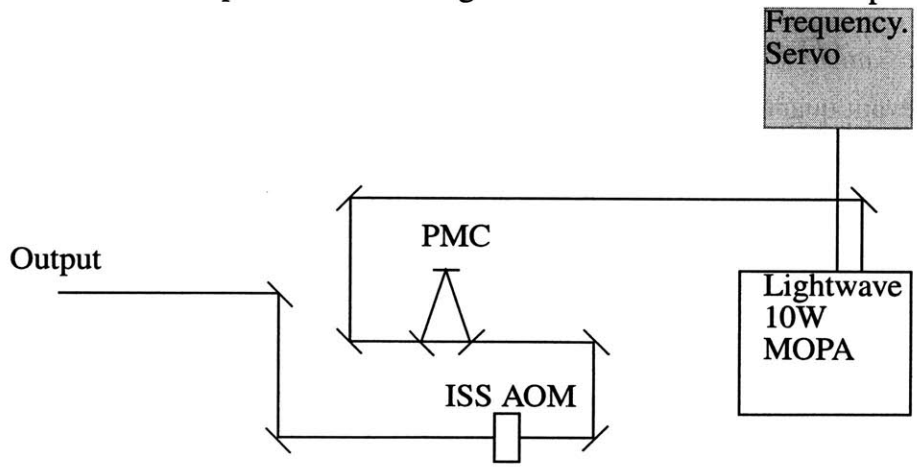

Figure 3.8: Schematic setup of the PSL during the intensity noise measurements.

adjusted to their nominal values. Of particular note is that the intensity servo acousto optic modulator was located after the pre-modecleaner.

We take both power spectra and power spectral densities with an HP 4395A Network/Spectrum analyzer. We distinguish between the two for the following reason: in 'Spectrum mode' the analyzer uses a peak-detect algorithm that yields a noise spectral density that can be up to 6dB higher than a 'Noise mode' measurement of the same signal. Also, in 'Noise mode' the analyzer

picks discrete frequencies to measure at, missing peaks that fall between these points (depending on the resolution bandwidth used). Therefore, for a quantitative measure of spectral noise we use the 'Noise mode' and to search for peaks we use 'Spectrum mode'. All power spectra are taken in linear frequency axis mode (the only mode supported by the analyzer) with 801 data points. We choose two frequency bands, 0-10 MHz and 10-100MHz, for measuring all signals. From 0 to 10MHz we use a single zero filter (a 200pF capacitor in series with the analyzer input) to whiten the signal thereby avoiding overloading the analyzer input stage or having to raise the input attenuation. In addition to the two frequency intervals, we take spectra centered on some of the larger peaks we observe.

With this setup we have filtered and unfiltered output signals and noise levels. They are dark noise,

$$Dark(f) = \sqrt{n_D^2(f) + n_{HP}^2(f)}. \tag{3.3}$$

dark noise with whitening filter,

$$Dark_{filt}(f) = \sqrt{n_D^2(f)F^2(f) + n_{HP}^2(f)} \tag{3.4}$$

measured signal,

$$V_{out}(f) = \sqrt{R^2H^2(f)[P_v^2(f) + P_{Shot}^2(f)] + n_D^2(f) + n_{HP}^2(f)} \tag{3.5}$$

measured signal with whitening filter,

$$V_{out-filt}(f) = \sqrt{\{R^2H^2(f)[P_v^2(f) + P_{Shot}^2(f)] + n_D^2(f)\}F^2(f) + n_{HP}^2(f)} \tag{3.6}$$

where the relevant quantities are:

$n_D(f)$: spectral density of the noise in the detector ($V/\sqrt{Hz}$).

$n_{HP}(f)$: spectral density of the noise in the analyzer ($V/\sqrt{Hz}$).

$P_v(f)$: spectral density of intensity noise ("technical", i.e. not shot noise) in the sampled beam ($W/\sqrt{Hz}$).

$P_{Shot}(f)$: spectral density of shot noise of the sampled beam ($W/\sqrt{Hz}$).

R: Responsivity of the photodiode (A/W).

$H(f)$: Transfer function of the detector (V/A).

$F(f)$: Transfer function of the whitening filter.

3.4.1 Results

The power in the sampled beam is adjusted so that we always have 100mA of photocurrent in the detector. This corresponds to about 142 mW of optical power. Figure 3.9 shows a composite

of the spectrum measurements, with detector noise subtracted.The slight rise in the curves at

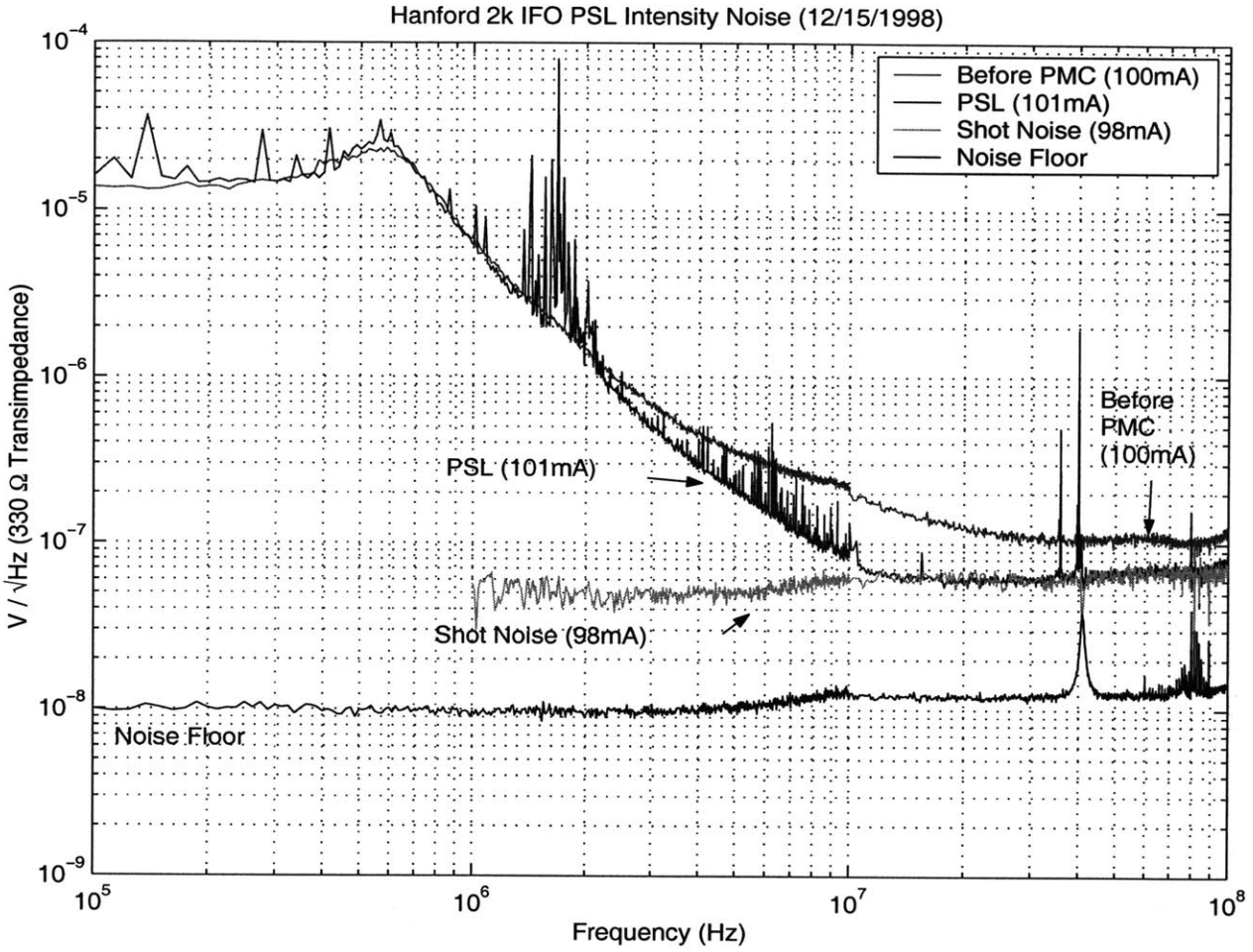

Figure 3.9: Intensity noise spectrum of the Hanford 2k PSL on 15 Dec 1998. Also shown are the shot noise level for the same amount of light and the dark noise level for the detector.

10MHz might be due to improper impedance matching of the whitening filter. We also include plots of the above spectra on a linear frequency scale, as they were taken (figures 3.10 and 3.11). In comparison, the 'spectrum mode' spectra of the PSL output in figures 3.12 and 3.13 reveal a larger density of peaks at frequencies less than 10MHz. We attribute the forrest of peaks in the noise up to 10 MHz to the PMC and the intensity servo (ISS) since they are absent in the spectrum of light taken before the PMC. The broad peak at 600kHz is due to the laser relaxation oscillation (which is actually damped by the master oscillator electronics). The 21.5MHz (figure 3.13) peak is from the PDH modulation used to lock to the frequency servo to the reference cavity. The 35.5 MHz peak is due to the PDH locking modulation for the PMC; the sidebands from the 74 kHz piezo resonance [PSL FDD] of the attached mirror are clearly seen on the 35.5 MHz carrier in the spectrum taken after the PMC (figure 3.14). The 43 MHz and 71 MHz peaks are harmonics of the 21.5 MHz and 35.5 MHz signals. The 40 Mhz peak is due to the drive frequency of the intensity servo acousto optic modulator and thus shows up only in the light after the PMC. The 80 MHz

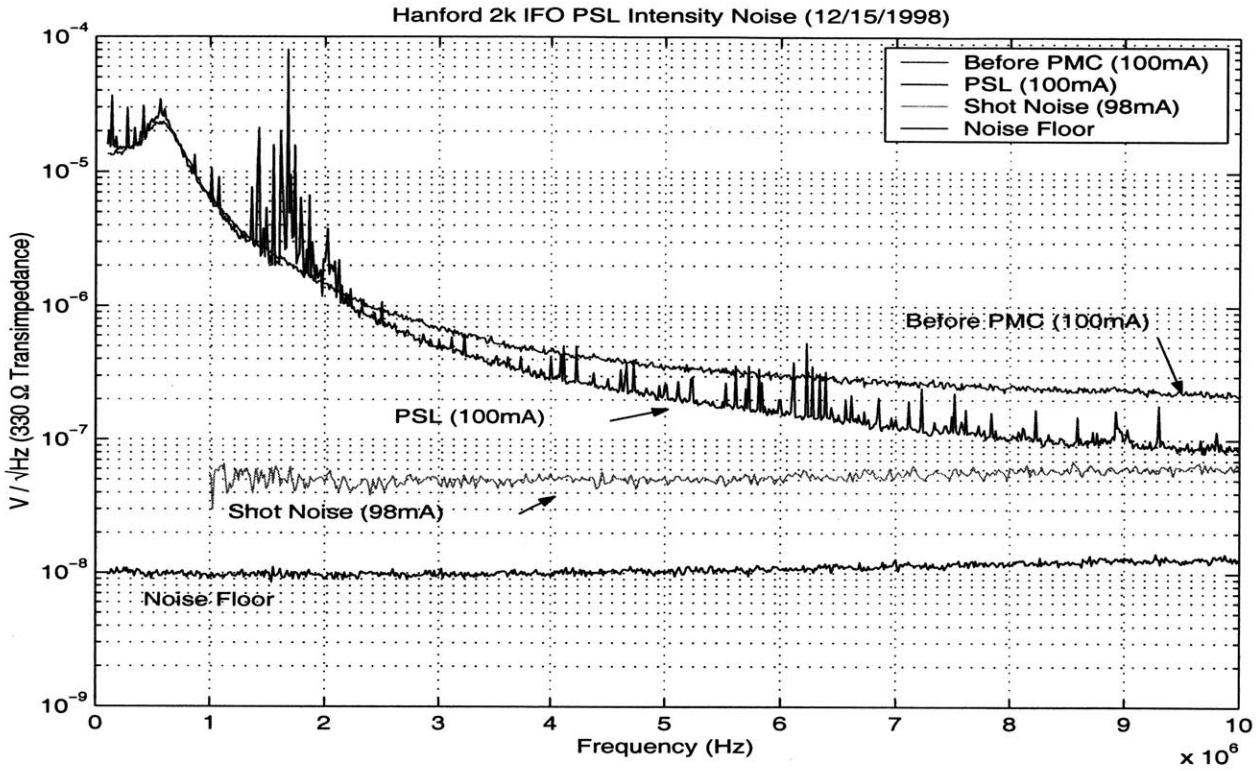

Figure 3.10: PSL intensity noise spectra. (0-10 MHz)

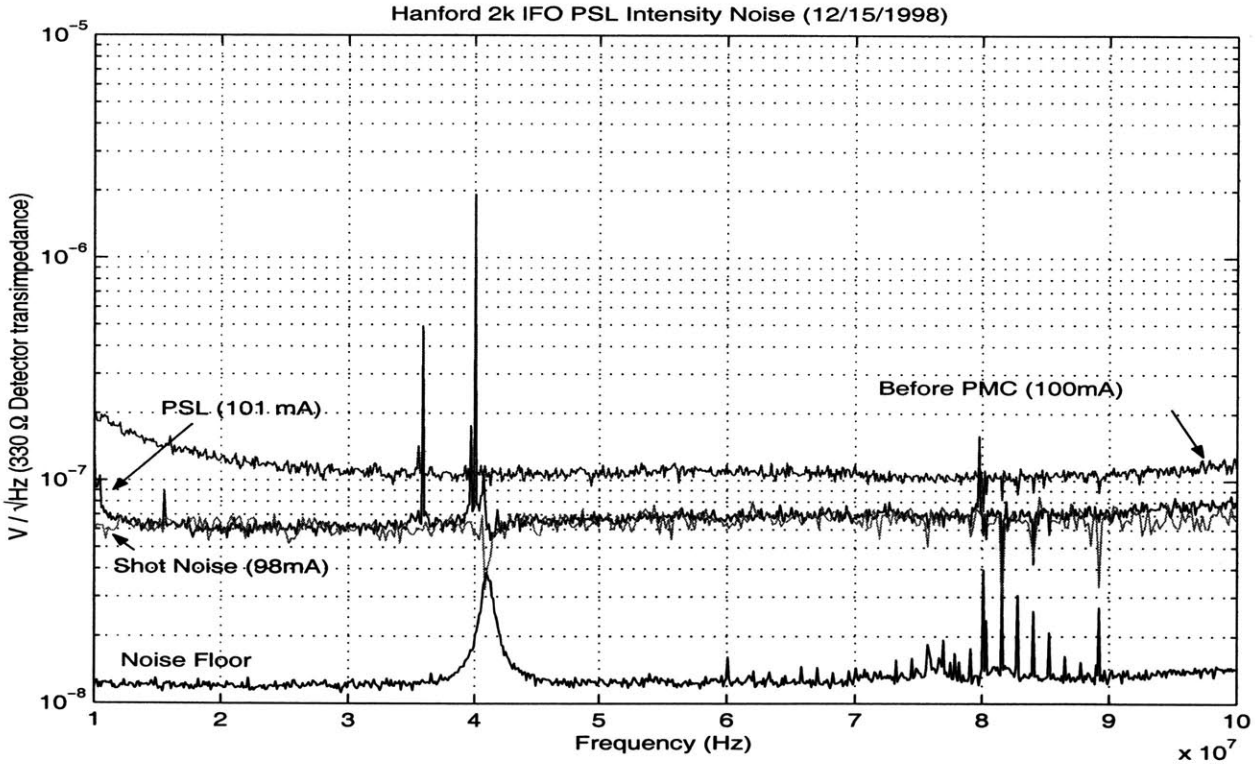

Figure 3.11: PSL intensity noise spectra. (10-100 MHz)

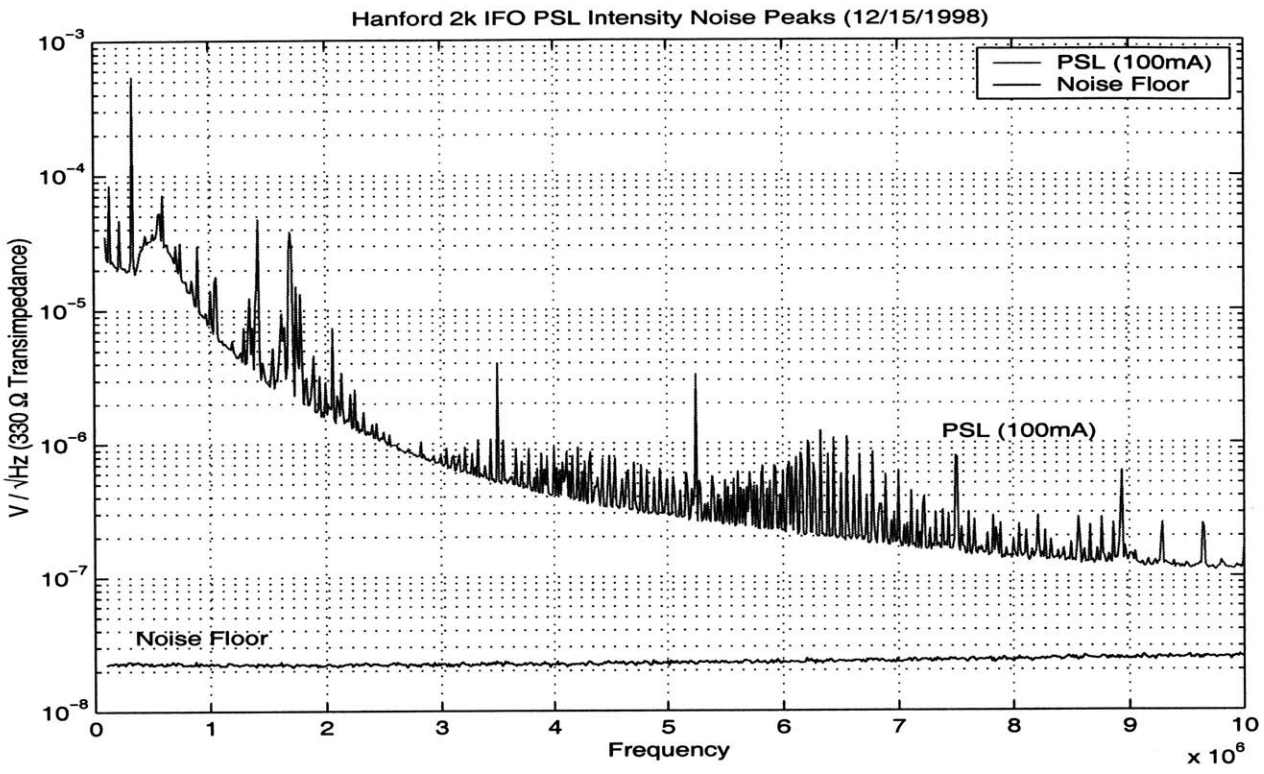

Figure 3.12: 0-10 MHz intensity noise in the PSL output.

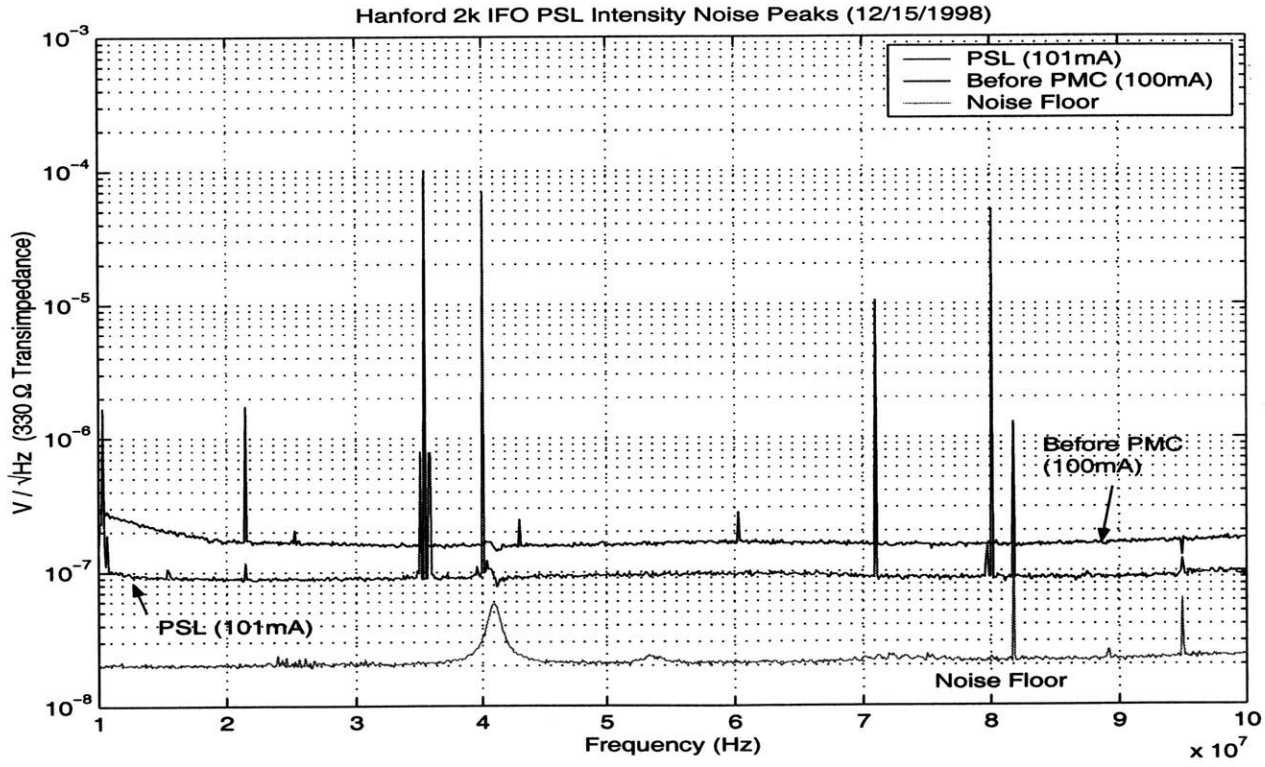

Figure 3.13: 10-100 MHz intensity noise of the PSL. (Spectrum Mode)

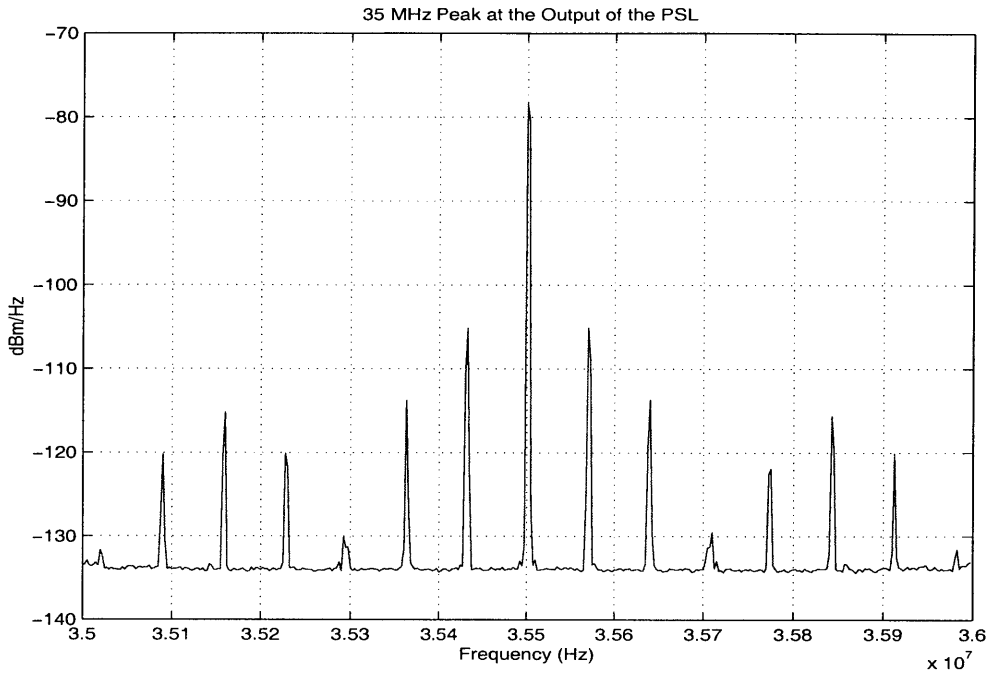

Figure 3.14: 35.5 MHz peak in the PSL output with sidebands due to PMC resonances. (The level is as measured at the output of the detector, i.e. there is no correction for response and gain in this figure).

peak is an harmonic of this. The 82 MHz line could be due to electromagnetic interference since it is seen in the dark level, perhaps from the voltage controlled oscillator (VCO) that drives an acousto-optic modulator in the frequency servo, but probably not to an on-air TV station (82 MHz is in the channel 6 band and the FCC reports channel 6 stations only in Spokane, Portland, Boise, none broadcasting more than 100 kW and all being fairly distant). The small peaks at 25 MHz and 60.5 MHz are unexplained, but they are clearly filtered out by the PMC. In the dark noise level of the 'noise mode' spectra (figures 3.9 and 3.11, both showing the same data), we see a set of peaks near 80 MHz. We suspect these are due to electromagnetic interference from a free running and unterminated VCO driver. This would have been possible since the PSL did not need to be locked and running for the dark spectrum measurement. Furthermore, these peaks are absent in the the 'spectrum mode' dark noise (figure 3.13) and absent in the measured light spectra as is evident from the downward spikes due to subtracting the dark noise.

3.5 Results

3.5.1 PSL Topology

We find a lot of peaks at frequencies up to 10MHz in the PSL output which are notably absent from the spectra of light incident on the pre-modecleaner. We suspect that they are due to the placement of the intensity servo acousto-optic modulator at the PSL output. This element should be placed before the PMC. It is also possible that some of the noise is due to the PMC itself; simply making the measurement without operating the ISS would clear up this possibility.

3.5.2 PMC performance

By dividing the noise spectrum of the light at the PSL output by the spectrum incident on the PMC, we find the transfer function for intensity noise of the PMC. The bandwidth of the cavity as

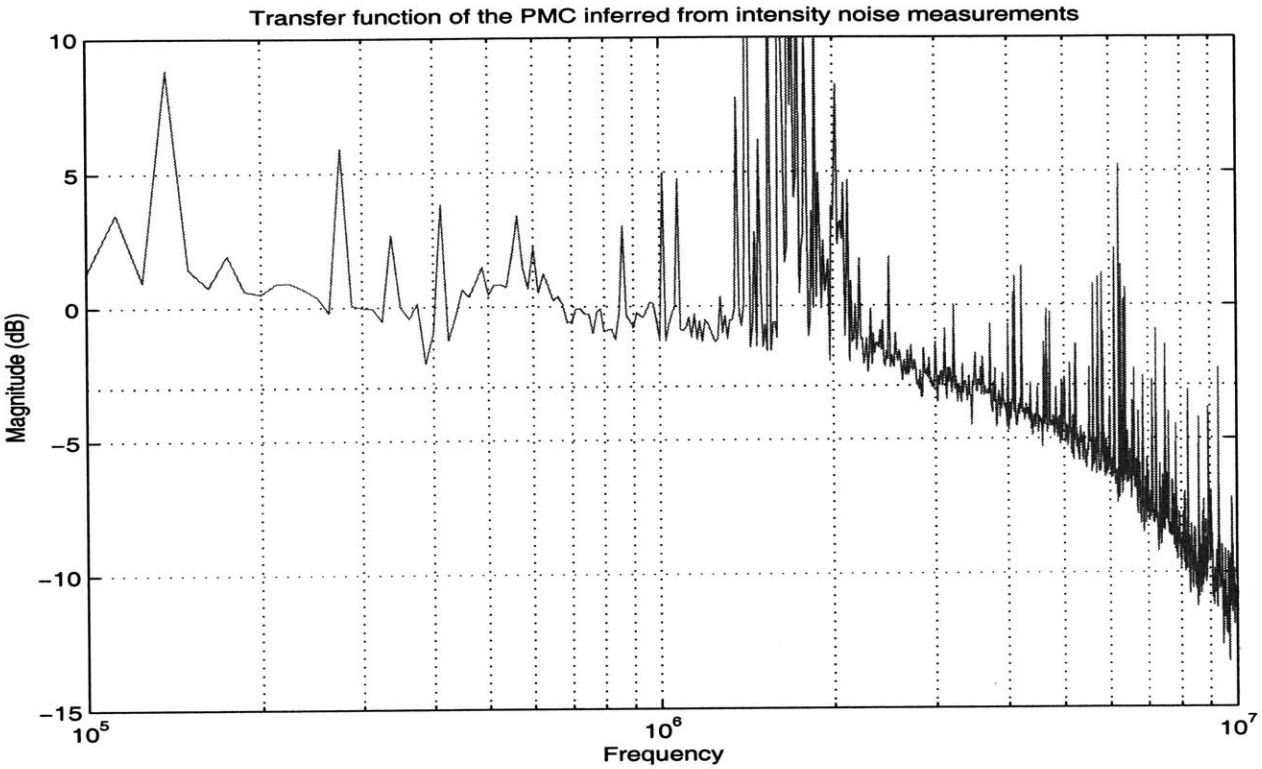

Figure 3.15: PMC transfer function derived from spectrum measurements. The extra dotted line is at the -3dB level.

seen from figure 3.15 is close to the designed 3.3 MHz [PSL CDD]. (The noisiness of this curve is due to the noise in the PSL output mentioned above).

3.5.3 Intensity Noise at the Modulation Frequency

We extrapolate the measured PSL noise spectrum between 3 MHz and 8.5 MHz up to the LSC modulation frequency of 24.5 MHz to estimate the noise for a 600mW beam. We first subtract the shot noise contribution and then remove the peaks in the noise spectrum using a simple algorithm that allows successive data points to differ in value by some maximal amount. We then make a linear log-log fit. The results are shown in figure 3.16. If we now assume that the non-shot noise component of the intensity noise scales linearly with power, we can make an estimate for the noise of a 600mW beam: at 24.5 MHz, for 142mW of optical power, the fit to the intensity noise spectrum gives $1.3 \times 10^{-8} V/\sqrt{Hz}$ of detected signal, and the shot noise is $6.2 \times 10^{-8} V/\sqrt{Hz}$. Scaling the fitted value by $600/142 = 4.2$ and the shot noise by the square-root of this value (2.05), we estimate the ratio of noise spectral densities will be:

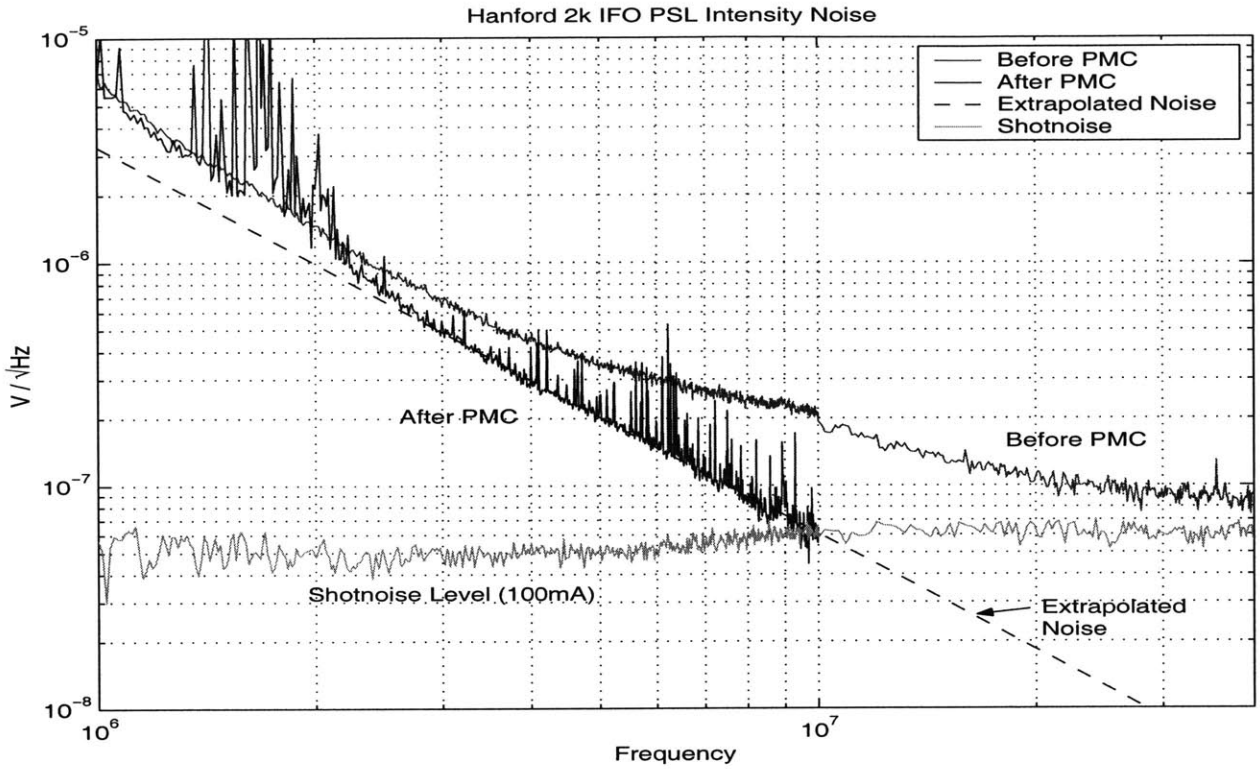

Figure 3.16: Extrapolation of the intensity noise to higher frequencies.

$$\frac{P_{\nu}^{600mW}(f)}{P_{shot}^{600mW}(f)} = 0.43 \tag{3.7}$$

This means that, at the output of the PSL, the shot noise is only 3.7 dB above the laser noise, or that the output noise is 1.09 times the shot noise limit of 600mW, exceeding the specification of 1.005. We need an additional attenuation of approximately 6.3 dB. Moving the pre-modecleaner resonance to 2 MHz has been suggested [PSL CDD], which would yield an additional 8.6 dB of noise attenuation, satisfying the requirement. We think, however, that a measurement at the full 600 mW is warranted to show if the requirement is not met. The originally designed 3.3 MHz cavity bandwidth was made with the assumption of a shot-noise limited master oscillator, which turned out not to be the case at 25 MHz.

3.5.4 High Frequency Noise

The propagation of noise from the master oscillator through the power amplifier to the detected beam is described by the equation [PSL CDD]

$$\left(\frac{P_{output}(f)}{P_{shot}(f)}\right)^2 = 1 + \eta\left\{H\left[\left(\frac{P_{\nu}^{MO}(f)}{P_{shot}^{MO}(f)}\right)^2 + 1\right] - 2\right\} \tag{3.8}$$

Here $P_{output}(f)$ is the amplitude spectral density of intensity noise at the output of the system, $P_{\nu}^{MO}(f)$ is the amplitude spectral density of intensity noise of the master oscillator, H is the

power gain of the amplifier, and η is the fraction of light detected at the output.

Let us estimate the right hand side of the above equation for our setup. Looking at figure 3.13, and assuming that the master oscillator is shot noise limited between 45 MHz and 75 MHz (where the noise measured before the pre-modecleaner is spectrally flat) we take

$$\frac{P_{\nu}^{MO}(45MHz < f < 75MHz)}{P_{shot}^{MO}(45MHz < f < 75MHz)} = 1 . \tag{3.9}$$

We assume the MO power was approximately 500mW, the MOPA output about 10W, so we take H to be 20. For η we take the fraction of light measured (142mW/10W) times the diode quantum efficiency (82%) to get 0.0116. Thus we estimate the relative power fluctuations should be $P_{output}(f)/P_{shot}(f) \approx 1.20$ Taking the average of the spectra in figure 3.13 between 45 MHz and 75 MHz, we find the measured ratio to be 1.62. Although we made some crude approximations in some of the above parameters, it is hard to see how we can adjust them to come up with a ratio this high. Careful study in the future might reveal another source of noise.

Chapter 4

Conclusions

4.1 Photodetector Development

We have described the requirements and subsequent tests that led to the development of the LIGO dark port photodetectors. The project decided to use the EG&G 2mm InGaAs diode primarily because of its low junction capacitance which leads to a better signal-to-noise ratio than the next best candidate, the Hamamatsu 2mm diode. We believe that the photodetectors will meet the requirements of LIGO; indeed, a very similar detector in the Phase Noise Interferometer (PNI), operating under conditions close to those in LIGO, has produced the expected shot-noise limited spectrum between 200 Hz and 2 kHz. This puts tight constraints on such nonlinear behavior of the detector as intermodulation, upconversion and downconversion [LSC FDD]. The same detectors are also conveniently and successfully used in other applications, such as the detection of reflection locking signals in the PSL.

While the diode and the detector meet LIGO specifications, we see the need for further development. The advanced LIGO interferometer, currently in research phase, will employ optical powers an order of magnitude higher than the first generation LIGO. Consequently the expected dark port continuous power could be as high as 6W and the unlocking transients up to 30 J. To meet advanced noise baselines, backscatter and spatial uniformity will be expected to improve by a factor of ten and the quantum efficiency should reach 90% [LSC '98]. Aside from not meeting the latter three expectations, using a parallel combination of existing detectors would require close to 40 units. Instead, we see progress in the development of new diodes. A back-illuminated device, with a transparent, large area contact layer and a thick absorption region has been proposed to address concerns of ohmic contact losses, quantum efficiency, and high capacitance [Byer '97]. Larger detector area and lower ohmic losses will significantly extend the linear power handling regime of the devices.

4.2 PSL Noise

In measuring the intensity noise of the prestabilized laser, we developed a broadband, high power detector, with capabilities comparable to those developed by others with similar goals [Gray '98]. We found that the PSL intensity noise may be higher than allowed, however a conclusive test is advised, with four of our detectors operating in parallel. The problem itself could be alleviated by lowering the pre-modecleaner resonance frequency or perhaps by investigating the source of noise in the master oscillator and its propagation through the power amplifier. We also uncovered excess peaks in the noise spectrum after the PMC and intensity servo which we strongly suspect to be a product of the latter. One way to eliminate these would be an intensity

control based on the supply current to the laser diodes. An implementation using only a current shunt actuator was unsuccessful but integrating an active source, perhaps as part of the laser power supply, remains to be tried [Abbott '98]. Another solution would be to place the ISS acousto-optic element before the PMC which would then presumably filter out the peaks.

Appendix A

Circuit Diagrams

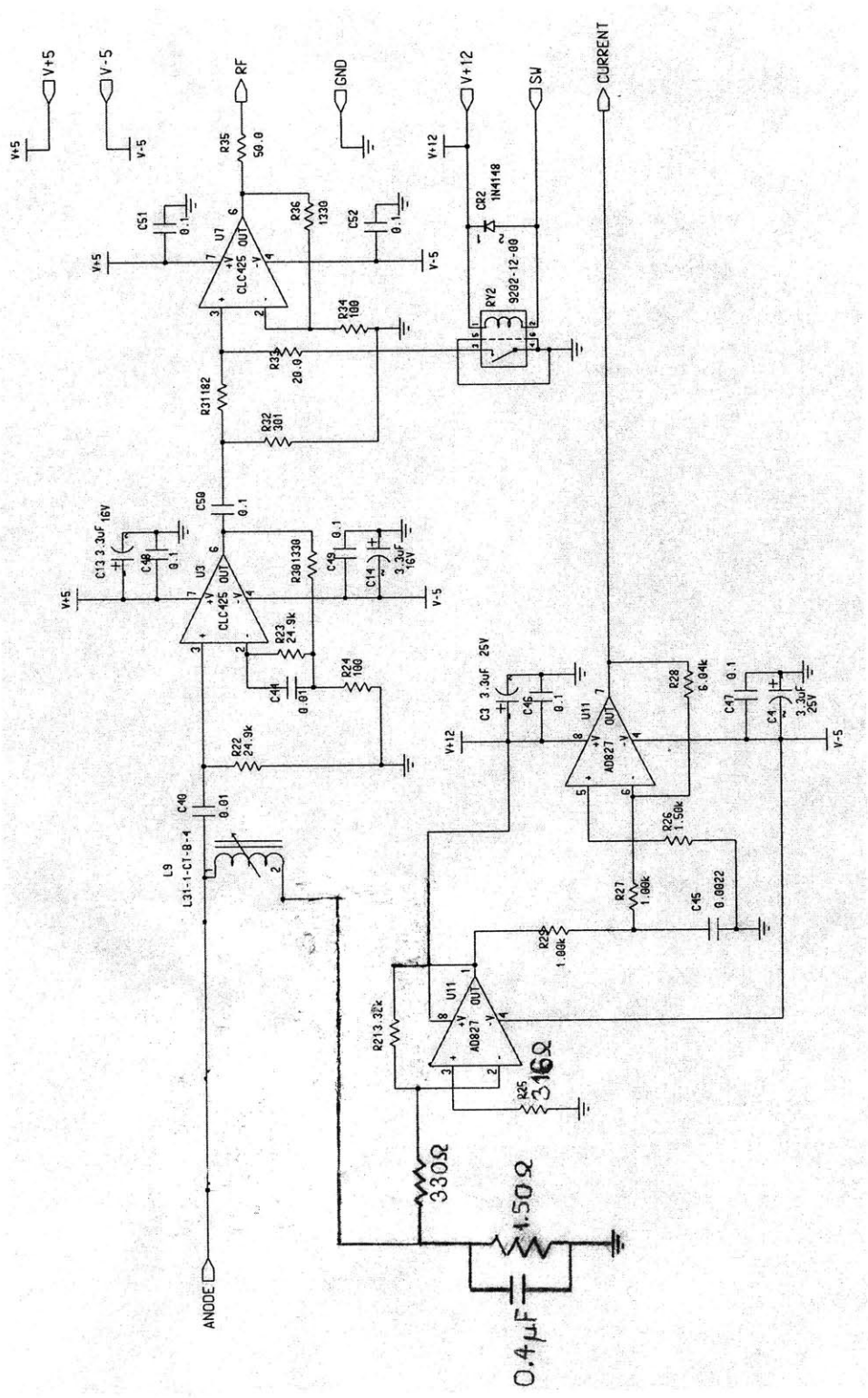

Figure A.1: Photodiode Test Circuit

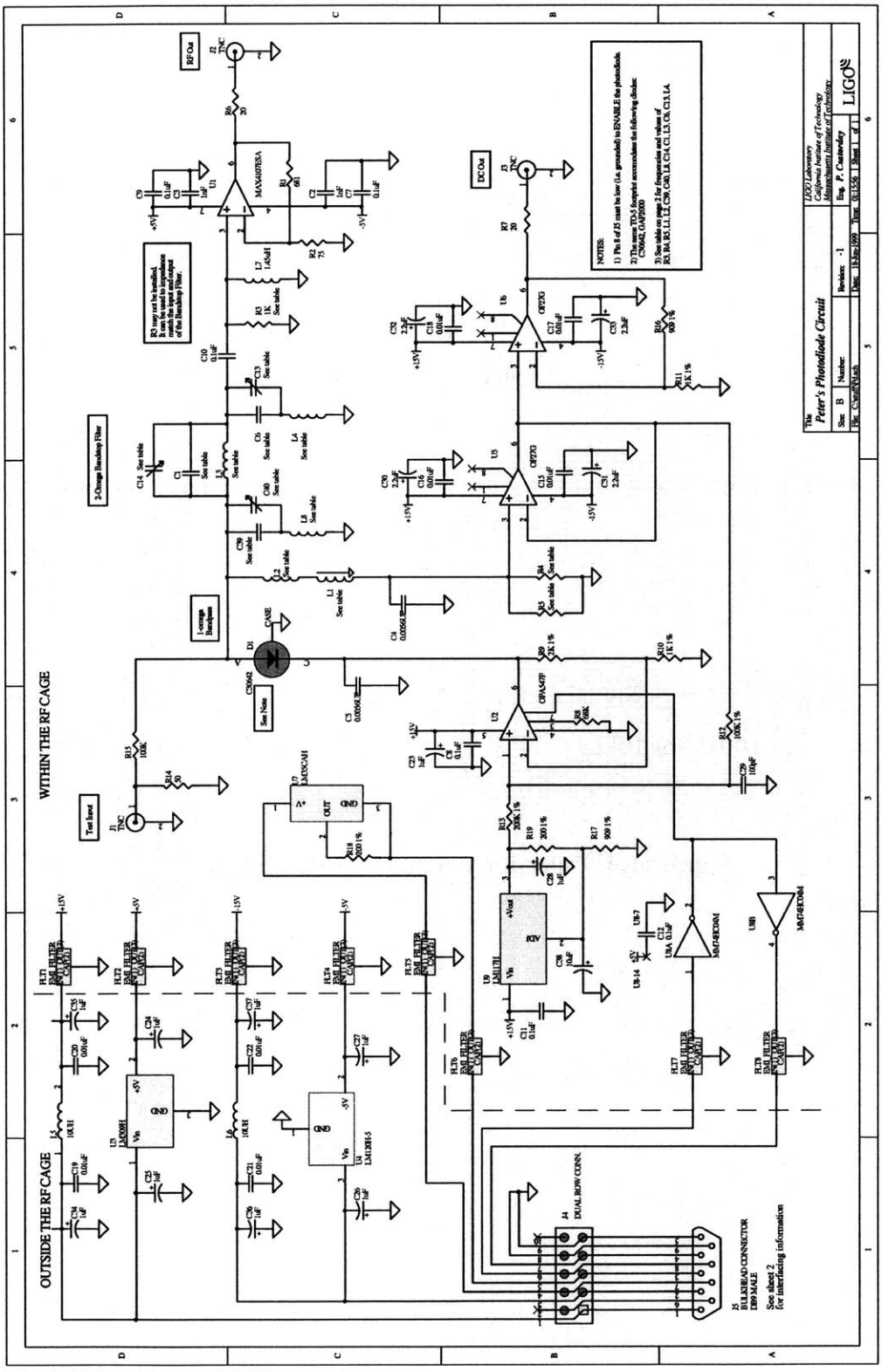

Figure A.2: LIGO RF Photodetector circuit.

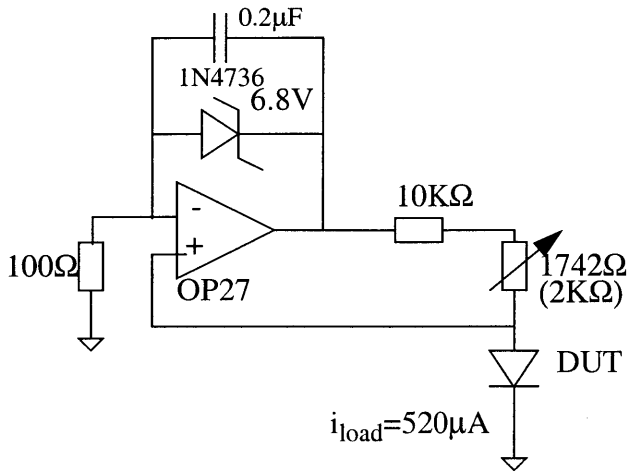

Figure A.3: Current source for the forward voltage drop measurements.

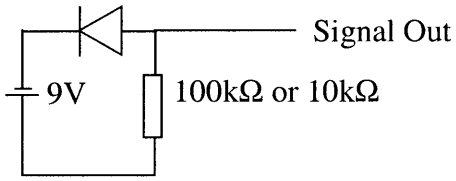

Figure A.4: Detection circuit for reflected light.

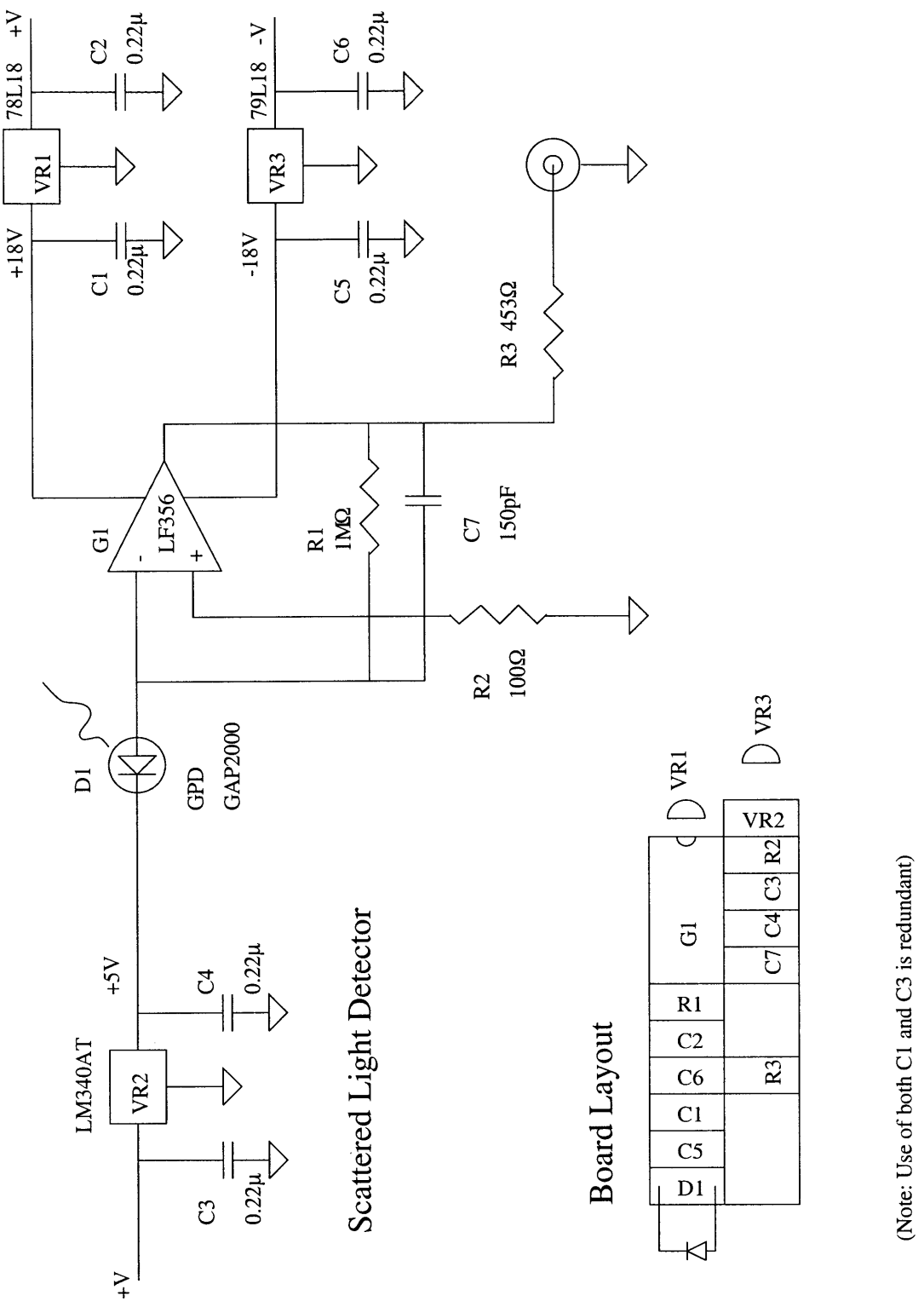

(Note: Use of both C1 and C3 is redundant)

Figure A.5: Scatterometer Detector Circuit

References

[Abbott '98] R. Abbott, private communication (1998)

[Abramovici '92] A. Abramovici, W. E. Althouse, R. W. P. Drever, Y. Gürsel, S. Kawamura, F. J. Raab, D. Shoemaker, L. Sievers, R. E. Spiro, K. S. Thorne, R. E. Vogt, R. Weiss, S. E. Whitcomb, and M. E. Zucker, "LIGO-The Laser Interferometer Gravitational-wave Observatory," *Science*, **256**, (1992) pp. 325-333.

[Bhattacharya '97] P. Bhattacharya, "Semiconductor Optoelectronic Devices", 2nd ed., Prentice Hall, (1997)

[Byer '97] R. Byer et. al., "A Supplemental Proposal for the GALILEO Program for a Collaboration with LIGO on Advanced Interferometer Development", unpublished, (1997)

[Byer '98] R. Byer, Lasers and Optics Working Group, LIGO Science Collaboration meeting, (1998)

[Deumié '96] C. Deumié, R. Richier, P. Dumas, C. Amra, "Multiscale roughness in optical multilayers: atomic force microscopy and light scattering", *Applied Optics*, Vol. 35, No. 28, (1996) pp. 5583-5594

[Drever '83] R. W. P. Drever, J. L. Hall, F. V. Kowalski, J. Hough, G. M. Ford, A. J. Munley, and H. Ward, "Laser Phase and Frequency Stabilization Using an Optical Resonator," *Appl. Phys. B*, **31**, (1983) pp. 97-105.

[Einstein '16] A. Einstein, "Näherungsweise Integration der Feldgleichungen der Gravitation," *Sitzungsberichte der Königlich Preussischen Akademie der Wissenschaften, Sitzung der physikalich-mathematischen Klasse*, (1916) pp. 688.

[Einstein '18] A. Einstein, "Über Gravitationswellen," *Sitzungsberichte der Königlich Preussischen Akademie der Wissenschaften, Sitzung der physikalich-mathematischen Klasse*, (1918) pp. 154.

[Gray '98] M. B. Gray, D. A. Shaddock, C. C. Harb, HA. Bachor, "Photodetector designs for low-noise, broadband, and high-power applications", Review of Scientific Instruments, **69,** 3755 (1998)

[LSC Photodiode] P. Csatorday, P. Fritschel, A. Marin, M. Zucker, "LSC Photodiode Selection", LIGO project document, T980016-00, (1998)

[LSC DRD] P. Fritschel, "Length Sensing and Control Design Requirements", LIGO project document T960058-03, (1997)

[LSC '98] LIGO Science Collaboration Lasers and Optics Working Group, "The Future of Advanced Research and Development in Lasers and Optics within the LIGO Science Collaboration", whitepaper, (3 September 1998)

[Mours '98] B. Mours, Private Communication, (1998)

[PSL CDD] R. Abbott, P. King, R. Savage, S. Seel, "PSL Conceptual Design", LIGO Project Document T970087-04, (1997)

[PSL DRD] P. King, R. Savage, S. Seel, "Pre-stabilized Laser Design Requirements", LIGO project document T970080-09, (1997)

[PSL FDD] R. Abbott, P. King, "Pre-stabilized Laser Final Design", LIGO project document T990035-00, (1999)

[Schnupp '86] L. Schnupp, unpublished, (1986)

[Sigg '97] D. Sigg, ed. "Frequency Response of the LIGO Interferometer", LIGO project document T970084-00, (1997)

[Stover '95] J. C. Stover, "Optical Scattering, Measurement and Analysis", 2nd ed., SPIE Optical Engineering Press, (1995)

[Weiss '99] R. Weiss, "Gravitational radiation," Reviews of Modern Physics, **71**, (1999) pp. S187-S196

[Zucker '98] P. Csatorday, A. Marin, M. Zucker, "Photodiodes for Initial and Advanced LIGO", LIGO project document G980022-00, (1998)

2727-56